Conduction Band-Edge States Associated With the Removal of d-State Degeneracies by the Jahn–Teller Effect

Gerald Lucovsky, C. C. Fulton, Y. Zhang, Y. Zou, J. Luning, L. F. Edge, J. L. Whitten, R. J. Nemanich, H. Ade, D. G. Schlom, V. V. Afanase'v, A. Stesmans, S. Zollner, D. Triyoso, and B. R. Rogers

Invited Paper

***Abstract*—X-ray absorption spectroscopy (XAS) is used to study band edge electronic structure of high-κ transition metal (TM) and trivalent lanthanide rare earth (RE) oxide gate dielectrics. The lowest conduction band d*-states in TiO_2, ZrO_2 and HfO_2 are correlated with: 1) features in the O K_1 edge, and 2) transitions from occupied Ti 2p, Zr 3p and Hf 4p states to empty Ti 3d-, Zr 4d-, and Hf 5d-states, respectively. The relative energies of d-state features indicate that the respective optical bandgaps, E_{opt} (or equivalently, E_g), and conduction band offset energy with respect to Si, E_B, scale monotonically with the d-state energies of the TM/RE atoms. The multiplicity of d-state features in the Ti $L_{2,3}$ spectrum of TiO_2, and in the derivative of the O K_1 spectra for ZrO_2 and HfO_2 indicate a removal of d-state degeneracies that results from a static Jahn–Teller effect in these nanocrystalline thin film oxides. Similar removals of d-state degeneracies are demonstrated for complex TM/RE oxides including Zr and Hf titanates, and La, Gd and Dy scandates. Analysis of XAS and band edge spectra indicate an additional band edge state that is assigned Jahn–Teller distortions at internal grain boundaries. These band edges defect states are electronically active in photoconductivity (PC), internal photoemission (IPE), and act as bulk traps in metal oxide semiconductor (MOS) devices, contributing to asymmetries in tunneling and Frenkel–Poole transport that have important consequences for performance and reliability in advanced Si devices.**

***Index Terms*—Complex oxides, conduction band edge states, d-state degeneracy, high-κ dielectrics, Jahn–Teller splittings, photoconductivity, spectroscopic ellipsometry, x-ray absorption spectroscopy.**

Manuscript received September 28, 2004; revised January 11, 2005. The work of G. Lucovsky was supported by the Office of Naval Research (ONR), the Air Force Office of Scientific Research (AFOSR), the Semiconductor Research Corporation (SRC), and the SRC/International SEMATECH Front End Processes (FEP) Center.

G. Lucovsky, C. C. Fulton, Y. Zhang, Y. Zou, R. J. Nemanich and H. Ade are with the Department of Physics, North Carolina State University, Raleigh, NC 27695 USA (e-mail: lucovsky@ncsu.edu).

J. Luning is with the Stanford Synchrotron Radiation Laboratories, Menlo Park, CA 94025 USA.

L. F. Edge and D. G. Schlom are with the Department of Materials Science and Engineering, Pennsylvania State University, State College, PA 16801 USA.

J. L. Whitten is with the Department of Chemistry, North Carolina State University, Raleigh, NC 27695 USA.

V. V. Afanase'v and A. Stesmans are with the Department of Physics, University of Leuven, Leuven, Belgium.

S. Zollner and D. Triyoso are with Freescale Semiconductor, Inc., Tempe, AZ 85284 USA.

B. R. Rogers is with the Department of Chemical Engineering, Vanderbilt University, Nashville, TN 37235 USA.

Digital Object Identifier 10.1109/TDMR.2005.845804

I. Introduction

THERE has been a search for alternative dielectrics with significantly increased dielectric constants, κ, with respect to SiO_2 to reduce direct tunneling in field effect transistors (FETs) with the equivalent oxide thickness, EOT < 1.5 nm. These substitutions for SiO_2 would allow relative increases in physical thickness proportional to κ for a given gate dielectric capacitance, thereby providing the possibility for significantly reducing direct tunneling. However, *increases* in κ are generally accompanied by *decreases* in the bandgap, E_{opt}, the conduction band offset energy, E_B, and the effective electron tunneling mass, m^*_{eff}, so that reductions in direct tunneling cannot be determined from increases in κ and physical thickness alone. These tradeoffs are quantified in a tunnelling figure of merit, Φ_m, given by

$$\Phi_m = k\left[E_B \cdot m^*_{eff}\right]^{0.5}. \tag{1}$$

This paper combines x-ray absorption spectroscopy (XAS) with other band edge spectroscopic studies to provide in information relative to the band edge states that determine E_{opt} and E_B. As such, the reported research results address intrinsic bonding effects that significantly limit integration of high-κ elemental oxides, e.g., HfO_2, into gate stacks for aggressively scaled Si complementary metal-oxide-semiconductor (CMOS) devices. These same limitations are alo studied in *complex oxides* comprised of transition metal (TM) oxides in combination with: 1) other TM oxides, such as in $HfTiO_4$ or $(HfO_2)_{1.0}(TiO_2)_{1.0}$; 2) trivalent lanthanide series rare earth (RE) oxides, such as $LaScO_3$ or $(La_2O_3)_{0.5}(Sc_2O_3)_{0.5}$; as well as 3) La and other RE/TM aluminates and silicates. One limitation relates to energies of the lowest d-state derived conduction bands relative to the conduction band edge of crystalline Si. This is designated as the conduction band offset energy, E_B, which defines the tunneling barrier at Si/high-κ dielectric interfaces. The high-κ TM metal oxides with the largest dielectric constants, k, relative to SiO_2, e.g., TiO_2, Ta_2O_5, etc., have the smallest optical bandgaps, E_{opt}, and conduction band offset energies [1], [2]. This paper demonstrates that calculated conduction band offset energies scale monotonically with calculated and/or measured optical bandgaps.

1530-4388/$20.00 © 2005 IEEE

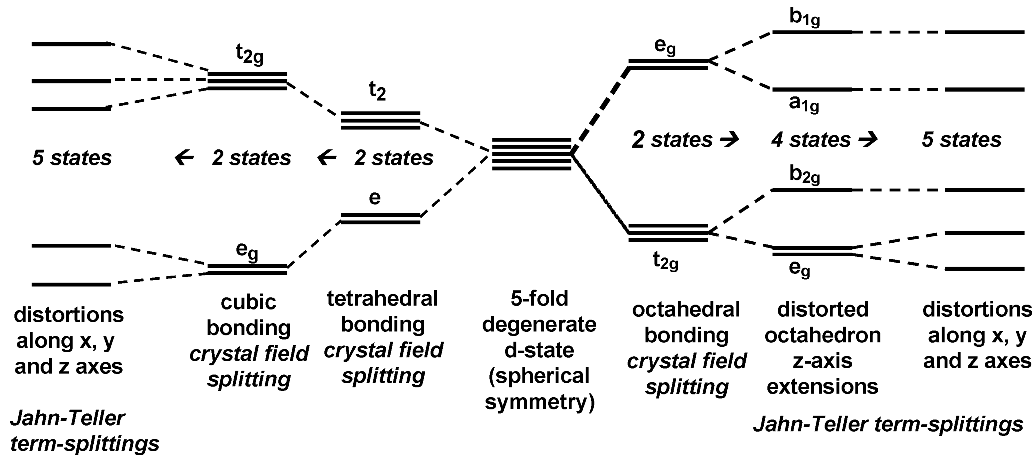

Fig. 1. Schematic representation of the transition from spherically symmetric d-state bonding, to crystal-field and Jahn–Teller degeneracy reductions.

The high-κ elemental oxides with the highest values of κ have conduction band offset energies that are too small, 1.0 eV, to satisfy projected tunneling leakage limits for scaled devices with EOT below 1.5 nm. One possible solution is to introduce these TM oxides into complex binary oxides, and increase conduction band offset energies through a coupling of the constituent oxide TM/RE atom d-states produced by bonding to a common O-atom. In contrast and based on O K_1 spectra of the constituent elemental oxides, the spectroscopic studies of this paper have identified more than two d-states in the complex oxides; however, their energies in O K_1 edge spectra suggest at most weak coupling between the d-states of the constituent TM atoms. On the other hand, the multiplicity of d-state features in the Ti and Sc $L_{2,3}$ edge spectra has suggested an alternative mechanism for the multiplicity of d-states found in the complex oxides as well.

This alternative mechanism derives from Jahn–Teller distortions that remove the degeneracies of the constituent atom valence and conduction band d-states through localized bonding distortions that are present in nanocrystalline, polycrystalline, and single crystalline complex oxides [3], [4]. These term-split d-states have been identified by x-ray absorption spectroscopy (XAS), as well as optical and uv absorption and ellipsometry. The removal of d-state degeneracies through bonding distortions that reduce local symmetry is the origin of large dynamic infrared (IR) charges, which lower frequencies of the IR active vibrations that contribute to the high values of κ in TiO_2, Ta_2O_5 and Sc_2O_3 [4]. This papers will demonstrate that Jahn–Teller term-split states, generated by larger bonding distortions at internal boundaries present in nanocrystalline dielectrics, generate localized states below the intrinsic conduction band edge d-states from the nanocrystallite grains, and that these localized states *are active* as interface and bulk traps in Si MOS devices, contributing to asymmetric shifts in field effect transistor (FET) threshold voltages, V_t, that degrade CMOS circuit operation.

Before addressing the XAS spectra, it is important to trace the *evolution* of the TM/RE d-states from the free atoms to the bonding environment of the oxides addressed in this review paper. The five-fold degeneracies of TM/RE d-states in an atom are partially removed by spin-orbit (S-O) splittings. These increase with increasing atomic number, z, and decreasing principal quantum number, n. For example, relatively deep core states such as the 3 d-state in Hf at ~1700 eV, have a S-O splitting of ~50 eV [5]. The S-O splitting in the valence 5 d-states in Hf is reduced to ~0.32 eV [5], and is the largest of the TM/RE elements addressed in this paper. For example, the S-O splittings of the Zr 4d, and Ti 3d states are 0.10 eV and 0.04 eV, respectively, and lower than the Hf 5d S-O splitting. In contrast crystal-field (C-F) splittings for symmetric six-fold and eight-fold bonding environments, typical of TM/RE atoms in elemental and complex oxides, are generally 2 to 3 eV. S-O splittings always result in lower energies for the doubly degenerate $d_{3/2}$ as compared to the triply degenerate $d_{5/2}$ atomic states, whereas C-F splittings are qualitatively different with the lowest conduction band d-states for six-fold coordination being derived from the $d_{5/2}$ atomic state, or equivalently, the triply degenerate T_{2g} state, and for eight-fold coordination from the $d_{3/2}$ atomic state, or equivalently, the doubly degenerate E_g state. Distortions in the six- or eight-fold coordinated bonding of the TM/RE atoms, that derive from the *static* J-T effect, either partially, or totally, remove the degeneracies of the E_g and T_{2g} states, resulting in at most five distinct d-states. The J-T term splittings depend on the *magnitude and symmetry* of the distortions, and are typically about 0.5–0.7 eV. It is also common practice to characterize the static J-T effect as a C-F effect resulting from a distorted local bonding geometry. The *J-T designation* gives additional insight into the mechanism that drives the degeneracy removal.

As noted above, the partial or complete removal of the E_g and T_{2g} degeneracies is determined by the nature of the distortion. For example, a symmetric *z* axis distortion of the octahedral bonding environment of a Ti atom (see Fig. 1), completely removes the degeneracy of the higher lying E_g states, but only partially removes the degeneracy of the lower lying T_{2g} state, whereas, a symmetric *z* axis distortion, coupled with the conversion of the *square* in the *x-y* plane to *rectangle* completely removes the degeneracies of both the E_g and T_{2g} states yielding five distinct d-states. Fig. 1 also includes a schematic representation for the S-O, C-F and J-T effects for four-fold coordinated atom in a tetrahedral, as well as eight-fold coordinated TM atoms, e.g., Zr or Hf, in cubic and distorted environments. This diagram provides a road-map for understanding the spectral features identified and discussed in the next few sections of this review. Since the d-state S-O splittings are generally small

relative to the C-F splittings, and the changes in these due to J-T effects, the S-O will be neglected in the discussions that follow.

II. Experimental Procedures

XAS measurements were performed at the National Synchrotron Light Source (NSLS) at the Brookhaven National Laboratory (BNL), and at the Stanford Synchrotron Radiation Laboratories (SSRL) at the Stanford Linear Accelerator Center (SLAC) using total photo-electron yield to determine the relative absorption strength of the spectral features associated with transitions from TM, RE, and O-atom core level states to empty conduction band-states [6]. Thin film samples of ZrO_2 and HfO_2 and their respective silicate alloys were prepared by remote plasma enhanced chemical vapor deposition (RPECVD) [7]. TiO_2 and $(Hf(Zr)O_2)_x(TiO_2)_{1-x}$ alloy thin films were prepared by physical deposition of Ti and Hf(Zr) atoms, followed by *in situ* plasma-assisted oxidation, and by reactive evaporation in an ultrahigh vacuum system in both instances using e-beam sources for the TM metals [8]. The growth of $GdScO_3$ and $DyScO_3$ single crystals has been discussed in [9]. Thin films of $LaAlO_3$, and $(La(Dy,Gd)_2O_3)_{1-x}(Sc_2O_3)_x$, were also grown by reactive evaporation in an ultrahigh vacuum deposition system using effusion cell sources for the TM and RE atoms [10].

III. X-Ray Absorption Spectroscopy Studies of Transition Metal-Oxide Films

A. Differences Between Intra- and Inter-Atomic Spectra

Fig. 2(a) and (b) presents Zr $M_{2,3}$ and O K_1 spectra for thin film nanocrystalline ZrO_2 [6]. The Zr $M_{2,3}$ spectrum in Fig. 2(a) is effectively an *intra-atomic spectrum* in which dipole-allowed transitions from *occupied* Zr core level, spin-orbit split 3p-states ($3p_{1/2}$ and $3p_{3/2}$) terminate in *empty* Zr 4d and 5 s states that lie well above the top of the valence band edge, ~5–6 eV. The energy differences between: 1) the spectral peaks of two 3d-states with triply degenerate E_g and doubly degenerate T_{2g} character, $\Delta(d_1, d_2)$, and 2) the spectral peak of the first 3d-state and the 4s-state $\Delta(d_1, s)$ are in good agreement (±0.3 eV) with *ab inito* calculations based on small clusters with central Zr atoms, and two shells of atomic neighbors [11]. The relative intensities of the 4d- and 5s-features are markedly different, and are consistent with the contributions of the Zr atomic radial wave functions of the initial and final states to the transition matrix element [12]. The *ab initio* calculations also provide equally good agreement with respect to the Zr-O bond length, and the spectral peaks of features in the valence band spectrum as determined by UV photoemission spectroscopy [8], [11].

The ZrO_2 O K_1 spectrum in Fig. 2(b) is an inter-atomic atomic spectrum with final states reflecting a mixing of O 2p*- and Zr 4d*-, 5s*- and 5p*-states. Agreement with *ab initio* calculations is approximately ±0.3 eV as well [11].

B. Intra- and Inter-Atomic Spectra for TiO_2, ZrO_2 and HfO_2

Qualitatively similar spectra have been obtained for the corresponding TM p-state and O atom core level absorption spectra in TiO_2 and HfO_2 [6]. These include the Ti $L_{2,3}$ and Hf $N_{2,3}$ spectra, as well the respective TiO_2 and HfO_2 O K_1 spectra. The Ti $L_{2,3}$ and O K_1 spectra for TiO_2 are displayed in Fig. 3(a) and (b), and the Hf $N_{2,3}$ and O K_1 spectra for HfO_2 are displayed in Fig. 4(a) and (b). Differentiated O K_1 spectra are displayed in Fig. 5(a) and (b) for ZrO_2 and HfO_2, respectively.

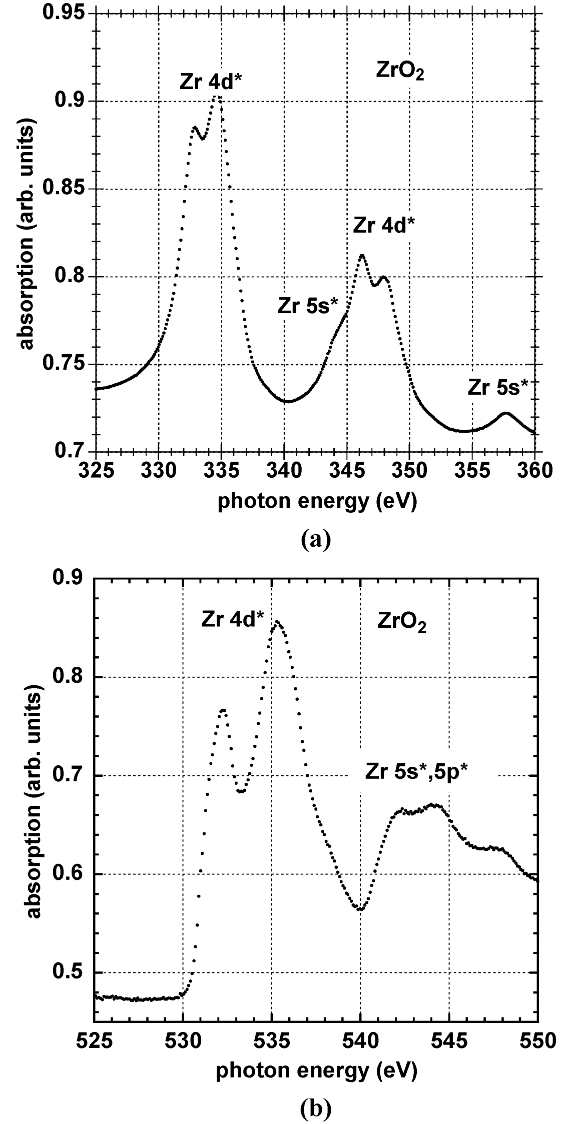

Fig. 2. Core level x-ray absorption spectra for nanocrystalline ZrO_2. (a) Zr $M_{2,3}$ spectra for excitation from spin-orbit split Zr 3p levels to empty Zr 4d* and 5s* states, and (b) O K_1 spectra for excitation from the O 1s level to molecular orbital Zr 4d* and 5s* states mixed with O 2p* states.

The relative intensities of features that terminate in empty d- and s-states, respectively, in Ti $L_{2,3}$, Zr $M_{2,3}$ and Hf $N_{2,3}$ spectra are consistent with the *intra-atomic* character of these transitions. This has been established by comparing the ratios of the integrated absorption of the d-state and s-state features in the respective L_3, M_3, and N_3 spectra with the transition probabilities for the corresponding Rydberg state transitions [12]. For example, this ratio is $\sim 3.0 \pm 0.3 \times 10^{-2}$ for 2p to 4s and 3d transitions in TiO_2, and increases to $8.9 \pm 0.9 \times 10^{-2}$ for 5s to 4d transitions in ZrO_2 [13]. The relative line-widths of the d features increase markedly as the atomic number, Z, of the transition metal atom increases. $Z = 22$ for Ti, 40 for Zr and 72 for

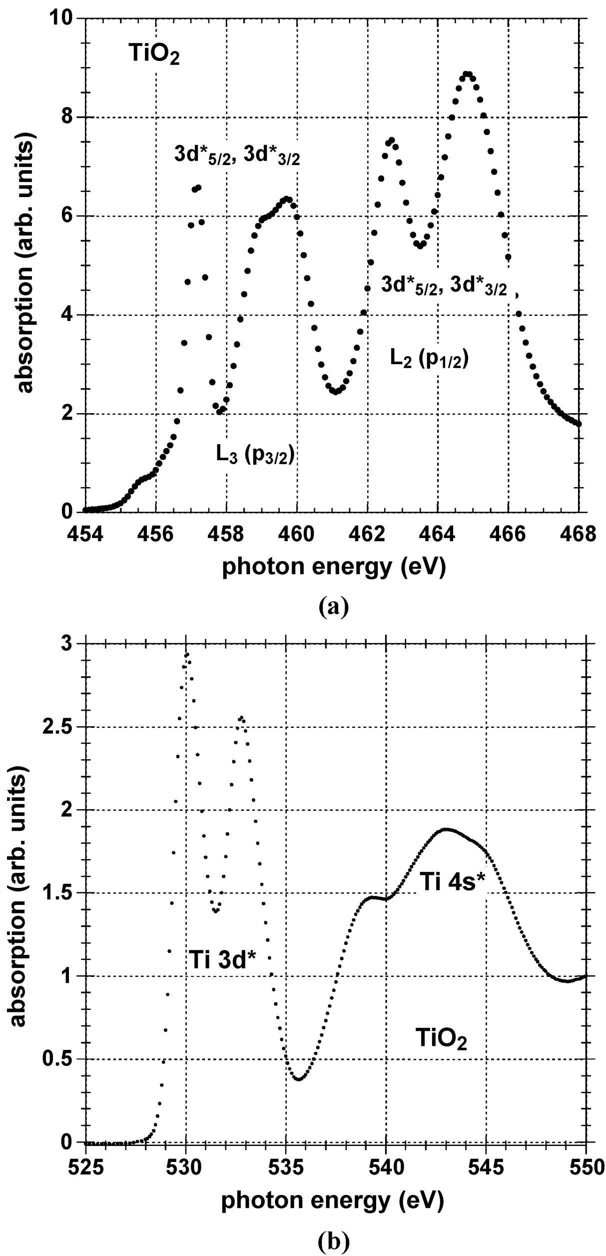

Fig. 3. Core level x-ray absorption spectra for nanocrystalline TiO_2. (a) Ti $L_{2,3}$ and (b) O K_1 spectra.

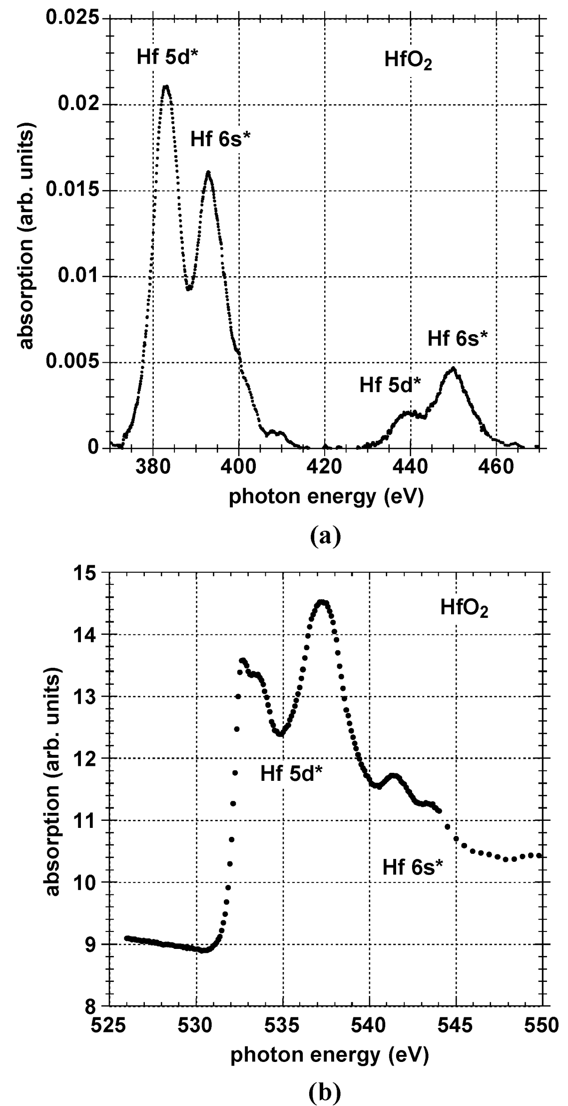

Fig. 4. Core level x-ray absorption spectra for nanocrystalline HfO_2. (a) Hf $N_{2,3}$ and (b) O K_1 spectra.

Hf, and following Slater's empirical rules for intra-atomic transitions, the line-width is expected to increase as Z^n, where $n \sim 2$ to 3 [13]. This broadening makes impossible to the resolve the doublet character of the 5d-state in HfO_2 in the intra-atomic N_3 transition. The 6s to 5d intensity ratio in the Hf N_3 spectrum is estimated to be ~0.9, or about an order of magnitude larger than the corresponding ratio for the Zr L_3 transition, again in good quantitative agreement with intensity ratios obtained for the Rydberg state transition probabilities [12].

The $\Delta(d_1, d_2)$ splittings for the *dominant* spectra features in the TiO_2 Ti $L_{2,3}$ and the ZrO_2 $M_{2,3}$ spectra are approximately the same, 2.0 ± 0.3 eV and 2.2 ± 0.3 eV, respectively, as are the corresponding $\Delta(d_1, s)$ splittings of 12.7 ± 0.3 eV and 11.8 ± 0.3 eV. The average $\Delta(d_1, s)$ splitting in HfO_2 is about 10 eV; if the $\Delta(d_1, d_2)$ splitting were about the same as in TiO_2 and ZrO_2, then this would increase the estimated splitting to about 11 eV. The splittings discussed above are associated with the local bonding symmetries and number of O-atom neighbors of the TM atoms in these thin film TM oxides which are six for TiO_2, and eight for ZrO_2 and HfO_2. Even though the coordinations of these atoms are different these d-state *crystal field splittings* remain the approximately the same.

The energy differences between the d_1 and s features these TM oxide spectra do not scale with the differences in the same atomic states in the $3(4,5)d^2 4(5,6)s^2 (nd^2 (n+1)s^2)$ representation appropriate to oxide bonding; ~5.0 eV for TiO_2, 2.8 eV for ZrO_2 and 2.4 eV for HfO_2; n is the principal quantum number [14]. The $\Delta(d_1, s)$ is approximately the same as in the L_3, M_3 and N_3 edge spectrum.

The O K_1 spectra are inherently *inter-atomic* in character, and the final states are better described by molecular orbitals (MOs) than empty states as in the p to d and s transitions discussed above [11], [15]. As already noted for ZrO_2, these MO final states mix O $2p^*$ anti-bonding states with anti-bonding Zr $4d^*$

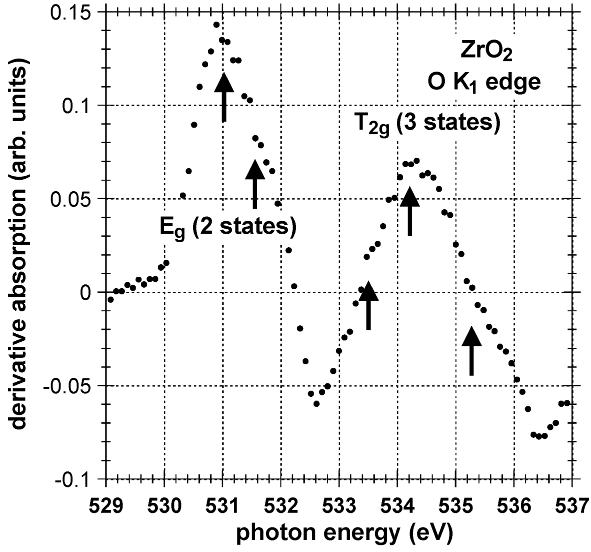

(a)

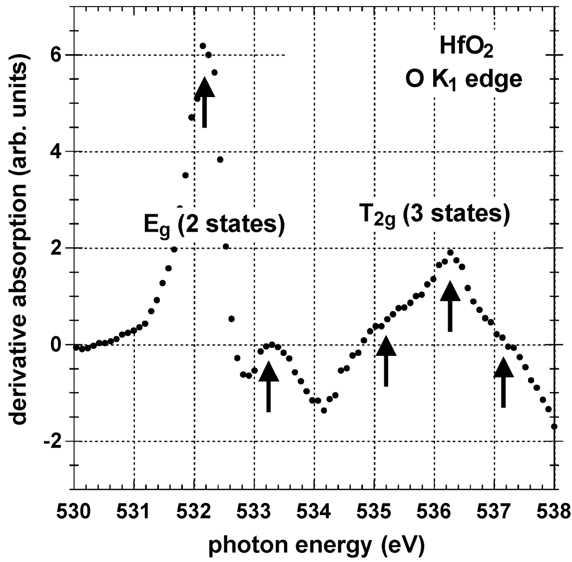

(b)

Fig. 5. Differentiated O K_1 spectra for (a) ZrO_2 and (b) HfO_2. The markers indicate the multiplicity of d^*-state features.

states, with transition matrix elements consistent with the symmetries of the MO initial and final states. These transitions display differences in the relative amplitudes of the doublet d^* features that are related to the six-fold coordination of Ti, and the eight-fold coordination of Zr and Hf. The T_{2g} or $d_{5/2}$ *triply degenerate states* contribute to the d_1 feature in TiO_2, whereas the E_g or $d_{3/2}$ *doubly degenerate states* contribute to the d_1 features in ZrO_2 and HfO_2. The $\Delta(d_1^*, d_2^*))$ splittings increase from 2.7 ± 0.2 eV in TiO_2, to in 3.2 ± 0.2 eV ZrO_2, and 4.3 ± 0.2 eV in HfO_2, while the $\Delta(d_1^*, s^*)$ splitting is 8, 4 ± 0.2 eV in TiO_2, and approximately the same in ZrO_2 and HfO_2, 10.1 ± 0.2 eV and 9.6 ± 0.2 eV, respectively.

Equally importantly, the differences in photon energy between the first d^*-state spectral peaks in the OK_1 spectra of TiO_2 at 530.1 ± 0.2 eV, ZrO_2 at 532.2 ± 0.2 eV, and HfO_2 at 532. eV, respectively, are the same to within an experimental uncertainty of ~0.3 eV as the differences in the experimentally

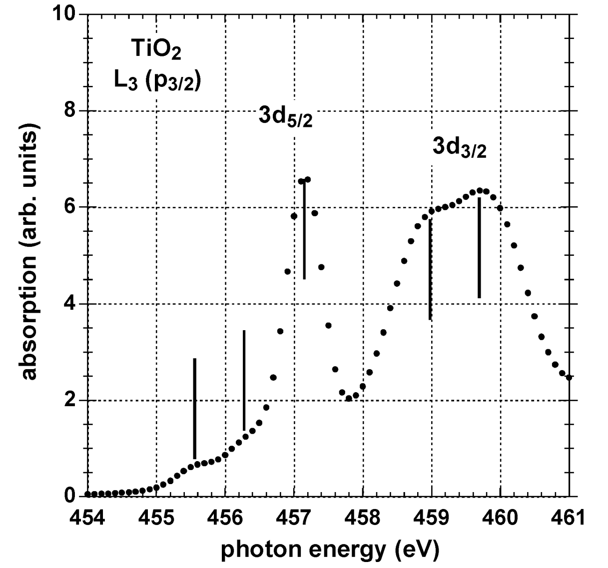

Fig. 6. Expanded *x* axis plot of the L_3 component of the $L_{2,3}$ spectrum of nanocrystalline TiO_2.

determined *optical bandgaps*, E_g, ~3.1 eV for TiO_2 ~ 5.6 eV for ZrO_2, and ~5.8 eV for HfO_2 [1], [2], [6], [15].

The correlation between the energies of the d_1^* features in the O K_1 spectra of TiO_2, ZrO_2 and HfO_2 and the energies of the atomic d-states for the electronic configuration appropriate to oxides, $nd^2(n+1)s^2$, where $n = 3$, 4 and 5, respectively for Ti, Zr and Hf [6], [14], has important implications for the scaling of these optical bandgaps, E_{gap}, and conduction band offset energies with respect to Si, defined here as E_B. This will be addressed in Section III-D. It is equally important to correlate features XAS spectra with photoconductivity (PC), internal photoemission (IPE) [16], and band edge dielectric functions and absorption obtained from spectroscopic ellipsometry (SE) studies, and this will be addressed later in this paper for both elemental and complex oxides.

C. Intra- and Inter-Atomic Spectra for TiO_2, ZrO_2 and HfO_2

Fig. 6 displays an expanded view of the L_3 spectrum of TiO_2. Combined with Fig. 5(a) and (b) which display differentiated spectra of the O K_1 edge spectra of ZrO_2 in Fig. 5(a) and HfO_2 in Fig. 5(b), these three spectra clearly indicate a multiplicity of five for the d-state features which is greater than what is expected from the *local bonding symmetry crystal field splitting* which predicts two features corresponding to one doubly degenerate and one triply degenerate state. To better understand the increased d-state multiplicity, the evolution the removal of d-state degeneracies with changes in the local bonding environments of the TM atoms in TM oxides has been presented in Fig. 1. This approach will also be useful in understanding the spectra of more complex oxides, comprised of TM oxides in combination with: 1) other TM oxides as in $HfZiO_4$; 2) lanthanide series rare earth (RE) oxides as in $GdScO_3$; and 3) nontransition metal oxides as $LaAlO_3$.

There are no symmetry driven splittings of TM/RE d-states in a spherically symmetric environment of nearest neighbor oxygen atoms, e.g., for a coordination number of twelve as in

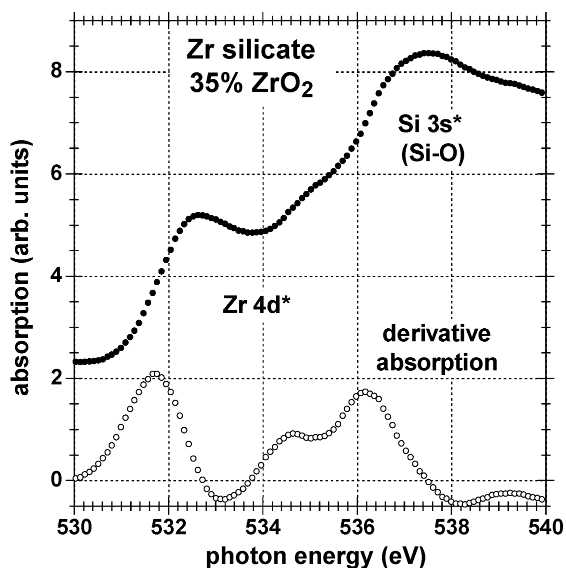

Fig. 7. O K_1 edge and differentiated O K_1 spectra for a noncrystalline Zr silicate alloy with ~60 molecular percent ZrO_2 : $(ZrO_2)_{0.6}(SiO_2)_{0.4}$. The dashed line markers indicate the positions of the spectral features in nanocrystalline ZrO2 thin films.

perovskite structure [4]. Stated differently the doubly degenerate $d_{3/2}$ and triply degenerate $d_{5/2}$ states are at the same energy giving rise to a d-state that is five fold degenerate. This degeneracy is removed in octahedral, tetragonal and cubic bonding environments as indicated in the diagram. The removal of this d-state degeneracy is generally designated as a *crystal field splitting*, and has been described at length in texts that have addressed TM/RE molecules and crystalline solids [3], [4], [15]. Other bonding environments with lower symmetry, such as the bonding of a TM atom at the center of a square also remove the degeneracies of the $d_{3/2}$ and $d_{5/2}$ states as well [15].

Crystal field splittings of the type described above are observed in noncrystalline Zr and Hf silicate alloys, and a representative O K_1 edge spectrum for a Zr silicate alloy ($\sim$ 35% ZrO_2) is presented in Fig. 7. There is no evidence in the absorption spectrum, or the derivative of the absorption spectrum of this representative silicate alloy for any additional d-state multiplicity indicative of a further removal of d-state degeneracy. The O K_1 spectrum (not shown) of this Zr silicate alloy indicates are reduction of the 4d-state line-width after an anneal at 900 °C which results in chemical phase separation into crystalline ZrO_2 and noncrystalline SiO_2 [7].

In marked contrast are the spectra in Figs. 6 and 5(a) and (b). Fig. 6 indicates the L_3 edge spectrum of TiO_2 in which five features are clearly evident. The number of distinct features in consistent with the complete removal of the $d_{5/2}$ and $d_{3/2}$ degeneracies. The lower energy T_{2g} triplet displays approximately equal splittings of 0.75 ± 0.5 eV between these three states, and the higher energy E_g doublet has an approximate splitting of 0.8 ± 0.2 eV. These term-splittings are consistent with the *distorted* octahedral bonding environment of Ti in crystalline TiO_2 with a rutile structure [3], [4], [11]. The octahedral arrangement of O atoms about the Ti atom displays a symmetric Ti-O bonding elongation of about 0.003 nm in the z-direction; the bonds in the *x-y* plane are the same length, but the square arrangement of an ideal octahedron in this plane is converted to a rectangle by an approximately seven degre (7°) bond angle change [11]. These degeneracy removals are commonly referred to as *static* Jahn–Teller term splittings, since the distortion increases the binding energy. This is contrast to dynamic Jahn–Teller splittings that occur during optical or near UV excitation [3], [15]. The increased bonding energy comes about because the number of d-electrons is two, and these occupy a lower energy state after the symmetric T_{2g} term splitting. These term splittings are not evident in the TiO_2 O K_1 edge spectrum of TiO_2, nor in the differentiation of the that spectrum as well, but as will discussed later on in this paper are clearly evident in both the photoconductivity response and in the dielectric constant and absorption constant extracted from spectroscopic ellipsometry measurements.

It is important to note that in nonmolecular solids, these term splittings can only occur in a crystalline environment because they require symmetry reductions that involve second neighbors as well. The Jahn–Teller term splittings can also be viewed as a special class of crystal field effects; however, this nomenclature does not provide an insight into the forces that contribute to the distorted bonding environment; i.e., an increase in binding energy associated with occupancy of the lowest term split state. The *evolution of symmetry reductions* that result from distortions of octahedral, as well as cubic and tetrahedral bonding in the context of the Jahn–Teller effect are displayed in Fig. 1, and include the octahedral and cubic distortions important for: 1) Ti and Sc, and 2) Zr and Hf, respectively.

In marked contrast to the results described above for TiO_2, the O K_1 derivative spectra in Fig. 5(a) and (b) indicate a complete removal of d-state degeneracies in nanocrystalline ZrO_2 and HfO_2, respectively. These degeneracy removals are not evident in the Zr M_3 and Hf N_3 spectra, consistent with a significantly longer core hole life-time associated with the O 1s state than for the Zr 3p and Hf 4p states. Core hole life-times scale inversely as the atomic number, Z^n, of the atom from which the excitation occurs, where $n \sim 2$–3.

Returning to the differentiated spectra in Fig. 5(a) and (b), the lower energy components of the d^*-state spectral features are split into two states and the higher frequency components into three states. This is consistent with the Jahn–Teller term splittings in cubic bonding environments in which there are distortions along all three principal axes. For distorted cubic bonding, the doublet E_g or $d_{3/2}$ state is lower in energy than the triplet T_{2g} or $d_{5/2}$ state, or exactly the reverse of the ordering in an octahedral environment with distortions along the three coordinate axes. The d-state splittings for HfO_2 are approximately 1.2 to 1.3 eV and larger by about 50% compared to those for TiO_2, providing a partial explanation for their observabilities in the O K_1 edge spectra.

Fig. 8 indicates the Jahn–Teller term splittings for ZrO_2 and HfO_2 spectral features in the O K_1 edge. This figure also includes the TiO_2 spectral features. For TiO_2, the highest energy state of the T_{2g} triplet in the Ti L_3 spectrum has been set equal to the lower energy $3d^*$ feature in the O K_1 spectrum. This approach is consistent with the spectra of Zr titanate alloys to be discussed in the next section of this paper. Finally, the average d^*-state energies obtained from this analysis of the respective

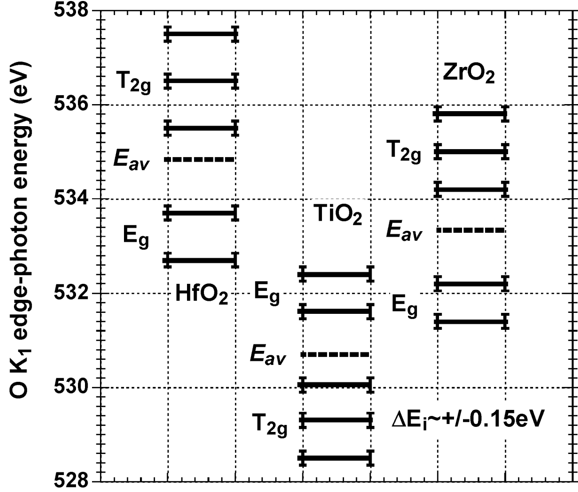

Fig. 8. Jahn–Teller term splittings for the ZrO_2 and HfO_2 spectral features in the O K_1 edge. This figure also includes the TiO_2 spectral features that have been scaled from the L_3 edge spectrum by equating the energies of the two strongest features in the TiO_2 O K_1 and L_3 spectra. The diagram also includes the average energies, E_{av}, of the respective d-state features.

O K_1 spectra scale monotonically with the atomic d-state energies of the atomic species, Ti, Zr, and Hf.

D. Band Gap and Conduction Band Offset Energy Scaling in Elemental Oxides: The Motivation for Studying Band Edge States in Complex Oxides

Robertson has developed a charge neutrality level (CNL) model for determination of conduction band offset energies for high-κ dielectrics formed on Si [2]. The results presented in [2] are plotted in this paper in Fig. 9 to reveal an approximately linear relationship for E_B as a function of E_{gap}. Fig. 9(a) and (b) contains plots, respectively, of: 1) E_B as a function of E_{gap}, and 2) E_{gap} and E_B as a functions of atomic d state energy for a representative set of TM oxides. The scaling in Fig. 9(b) follows directly from the spectroscopic results presented above, and from the *ab initio* calculations for O K_1 spectra that provide the correlation between optical bandgaps and atomic d-state energies [11]. A band offset energy of at least 1 eV, and more generally about 1.2 eV or more is required for tunneling/thermionic leakage current to be sufficiently low for scaled CMOS devices [17]. Using this criterion, the TM oxides with the highest dielectric constants, TiO_2, and Nb_2O_3 and Ta_2O_3, have offset energies below 1 eV that either correlate with high tunneling leakage, and/or electric field assisted injection into low-lying conduction band-states associated with these atoms, and are therefore not candidates for replacement dielectrics in scaled CMOS devices. Based on this scaling with atomic d-states, the elemental oxides of: 1) Zr and Hf and 2) Y, La and the lanthanide RE oxides are expected to have conduction band offset energies >1.2 eV, and therefore have the *potential* for meeting roadmap targets for low tunneling leakage current, provided that the electron tunneling mass, m_{eff}, does not decrease significantly with decreasing E_B, and mitigate gains for increases in κ [see (1)]. Since the TM and RE d-states do not mix with the lowest conduction band s-states of Si and Al, these scaling arguments can be extended to the silicate

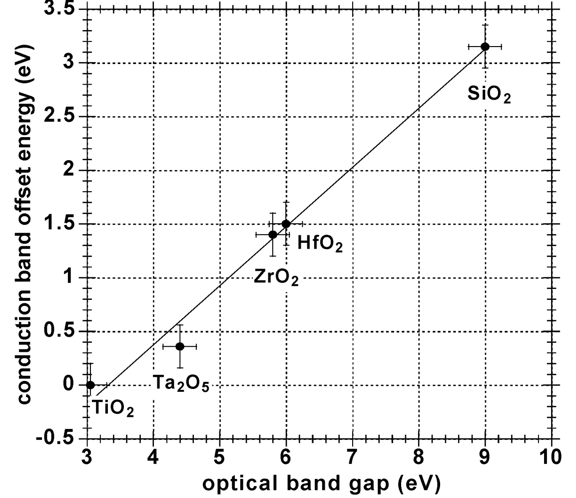

(a)

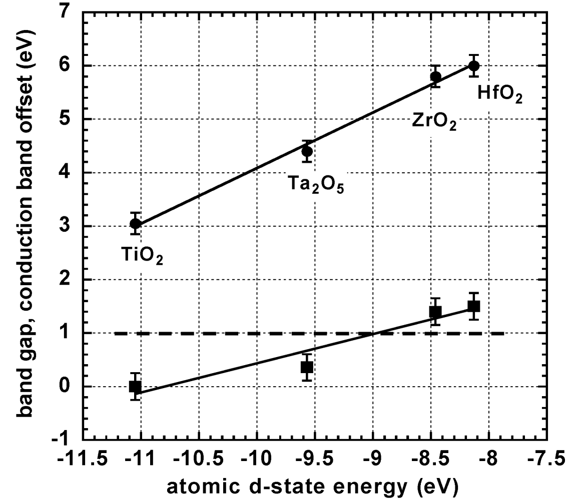

(b)

Fig. 9. (a) Conduction band offset energy, E_B, as a function of the optical bandgap, E_g, from the results presented in [2]. (b) E_g and E_B as a function of atomic d-state energy.

and aluminate alloys of the Zr, Hf, Y, La and the lanthanide RE atoms [7]. However, it must be recognized that there are many other factors that contribute to the integration of high-κ dielectrics into advanced Si devices [1]. These include process integration issues relative to thermal budgets, substitution of dual metal or single midgap metal gates for bulk and thin film Si on insulator devices, respectively, as well as other high-κ dielectric issues including: 1) internal dielectric interfaces with ultrathin interfacial SiO_2 layers [18], [19], and 2) intrinsic band edge traps addressed in this paper [20], [21].

The results presented above have raised an interesting question regarding the lowest energy d^*-states in complex oxides that include Sc and Ti, as for example stoichiometric and Zr and Hf titanates, and RE scandates such as La, Dy and Gd scandate: is it possible for d-states of the two TM atoms in the titanates, and the Sc and RE atoms of the scandates to *couple and mix* in ways that increase the optical bandgap, and the conduction band offset energies of these complex alloys? If this mixing were to occur this would then provide a way to obtain independent control of band offset energies and dielectric constants, and thereby

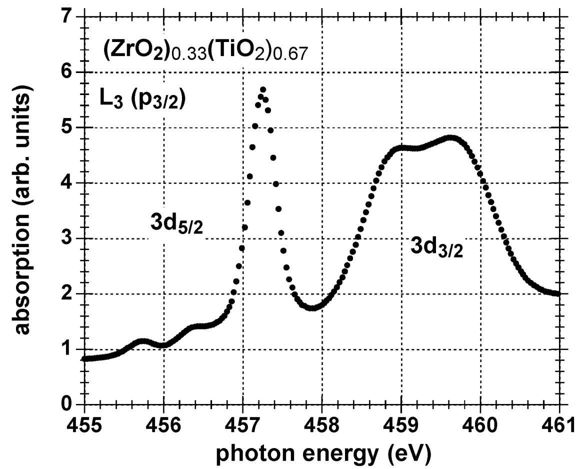

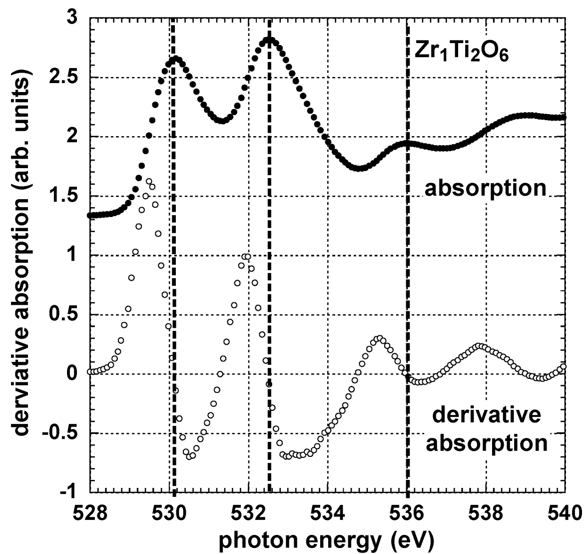

Fig. 10. Core level x-ray absorption spectra for *stoichiometric Zr titanate alloy* with a composition, $ZrTi_2O_6$ or $(ZrO_2)_{0.33}(TiO_2)_{0.67}$: (a) the Ti $L_{2,3}$ spectrum and (b) the O K_1 spectrum. The dashed lines in indicate the d^*-state features in the O K_1 spectrum in (b).

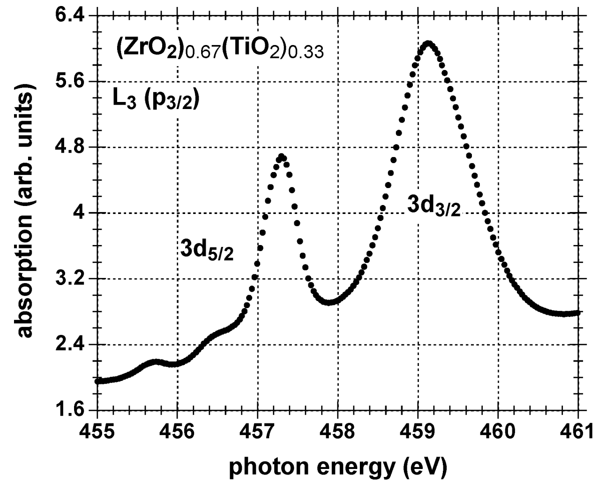

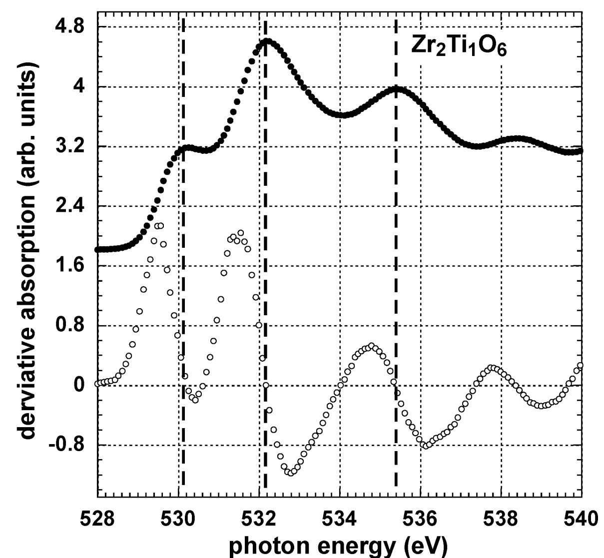

Fig. 11. Core level x-ray absorption spectra for *stoichiometric Zr titanate alloy* with a composition, Zr_2TiO_6 or $(ZrO_2)_{0.67}(TiO_2)_{0.33}$: (a) the Ti $L_{2,3}$ spectrum and (b) the O K_1 spectrum. The dashed lines in indicate the d^*-state features in the O K_1 spectrum in (b).

get around the limitations of Fig. 9(a) and (b). These issues are addressed in Section IV.

IV. Complex Oxides

There has been an increasing interest in stoichiometric complex oxides as high-κ dielectrics for scaled Si CMOS. These oxides are differentiated from TM/RE silicate and aluminates which are pseudo-binary alloys, e.g., $(ZrO_2)_x(SiO_2)_{1-x}$, in which the alloy compositions are varied continuously with the range, $1.0 > x > 0.0$. Two different alloy systems are addressed; these are: 1) Zr and Hf titanates, in which the values x for ZrO_2 and HfO_2 to $1 - x$ for TiO_2 have been restricted to compositional ratios of 1:2, 1:1 and 2:1, and 2) the stoichiometric RE scandates, e.g., $La(Dy, Gd)ScO_3$ in which the ratio of the elmental oxides, $La(Dy, Gd)_2O_3$ and Sc_2O_3 are 1:1.

Analysis of XAS spectra for these materials have demonstrates that there is very little coupling between the d-states of the constituent TM and/or RE d-states. To a very good approximation, the d-state features in the respective O K_1 edges are at energies which are closely coupled to their atomic d-state energies in the $nd^2(n+1)s^2$ representation for tetravalent group IVB, and in the $nd^1(n+1)s^2$ representation for trivalent TM and lanthanide series RE metals discussed above. This aspect of the spectra will be addressed with respect to the $ZrTi_2O_6$, Zr_2TiO_6, and $LaScO_3$ thin films discussed in Sections IV-A and IV-B.

A. Zr and Hf Titanates

Fig. 10(a) displays the L_3 Ti spectrum, and Fig. 10(b) the O K_1 spectrum for a *stoichiometric alloy* with a composition, $ZrTi_2O_6$. Fig. 11(a) and (b) displays the corresponding spectra for a second alloy with a composition Zr_2TiO_6. The O K_1 edge spectra in Figs. 10(b) and 11(b), respectively, indicate three distinct d^*-state spectral features, the energies of which are consistent with a *mixture of features* terminating in transitions to the respective Ti and Zr d-state at approximately: 1) 530.2 and

532.4 eV for TiO_2 and 2) 532.4 and 535.4 to 536.0 eV for ZrO_2, each with an experimental uncertainty of ±0.1 eV. This means that the lowest energy spectral feature is TiO_2-like, the highest spectral feature ZrO_2-like, and the middle frequency has contributions from both TiO_2 and ZrO_2. Derivative O K_1 spectra do not indicate and additional d^*-state spectral features. The respective Ti L_3 spectra in Figs. 10(a) and 11(a), provide evidence for Jahn–Teller term splittings indicating a complete removal of the Ti 3d state degeneracies. The presence of the term split features in the Ti L_3 spectra, and their absence in the respective O K_1 edge spectra is essentially the same behavior noted above for TiO_2 O K_1 and Ti L_3 spectra. The T_{2g} term-split energies of the three lower π-states in the Ti L_3 spectra are the same for each composition, whereas there are marked differences in the two E_g term-splitting of the σ-states. These are consistent with differences in the character of the bonding between Ti and its second neighbors: 1) a mixture of ionic and covalent bonding for a compositionally averaged mixture of Zr and Ti neighbors for $ZrTi_2O_6$, and 2) a more ionic bonding with a compositional average two Zr neighbors in Zr_2TiO_6 [3]. The second neighbor bonding has little effect on the T_{2g} π-bonding states which are localized on the nearest neighbor Ti and O, but has a strong influence on the E_g σ-bonding states which are significantly more delocalized.

The O K_1 spectra of Hf titanate alloys, $(HfO_2)_m(SiO_2)_n$, with: 1) $m = 1$, $n = 2$, $m = 1$, $n = 2$, and $m = 2$ and $n = 1$ display qualitatively and quantitative similar spectra to the Zr titanates discussed above. To a good approximation, the features in the O K_1 edge are also well described by a *mixture* of HfO_2 and TiO_2 features, with small shifts that are consistent with a weak coupling between Ti and Hf d-states with the same symmetries. This is illustrated in Fig. 12(a) and (b) for $HfTiO_4$, or the 1:1 composition: $(HfO_2)_1(SiO_2)_1$. The TM π-states that form the top of the valence band and the bottom of conduction band are predominantly Ti-like and are shifted by less than 0.5 eV from their values in the TiO_2, whereas there are larger shifts, ∼1 eV in the Hf-like σ-bond states that are at the bottom of the valence band higher in the conduction band. One explanation proposed for this behavior was that it was indicative of relatively weak coupling between the π-bonded states that are at the top of valence band, and stronger coupling between the σ-bonded states that are deeper in the valence band [8]. However, this explanation fails to take into account the strong contribution of O 2p nonbonding states at the top of the valence band [6]. On the other hand, the differences in the valence band states of the elemental and complex oxides are explained quantitatively by noting that the valence and conduction band spectra of the constituent elemental oxides, TiO_2 and HfO_2 include the effects of Jahn–Teller term splittings, whereas those of the complex oxide, $HfTiO_4$ include Jahn–Teller shifts for the Ti-atoms, but not the Hf-atoms. The ∼1 eV shifts of the states at the bottom of the valence band, and above the conduction band edge as revealed in the O K_1 spectrum. The smaller shifts in the states at the top of valence band and bottom of the conduction band may indeed be due to a weak coupling of π-bonded states; however, this will require additional study.

Similar valence band, and O K_1 edge shifts have been found in Zr titanate alloys, and additional compositions are being studied to see if the observed shifts correlate with Zr titanate phases, or mixtures of ZrO_2 and HfO_2. Stated otherwise, comparisons between Zr titanate alloys and the end-member oxides may prove to be a novel way of identifying compositions that correspond to stoichiometric complex oxides, as distinguished from alloys with random, or statistical bonding of the constituent elemental oxides.

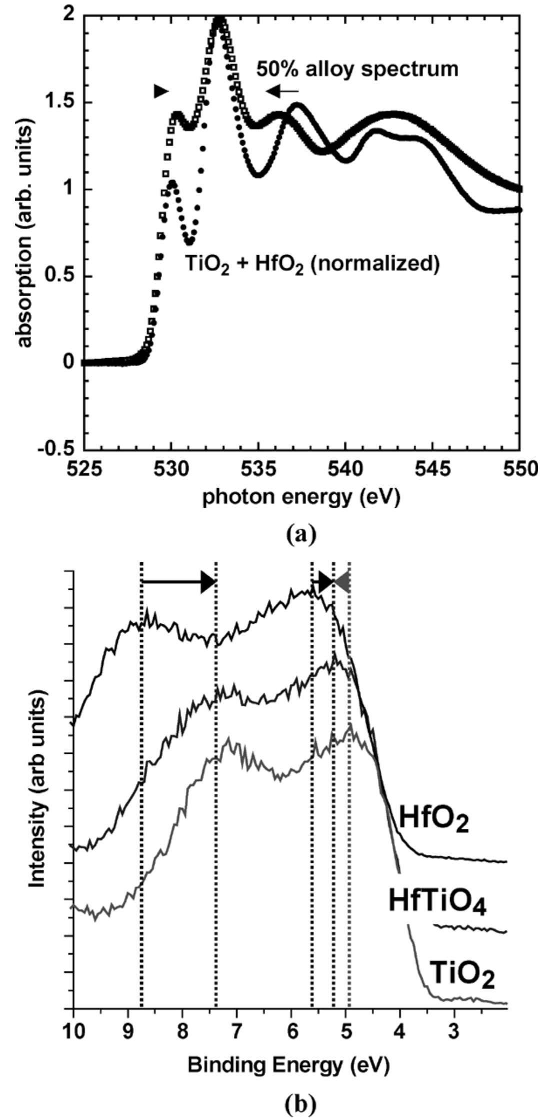

Fig. 12. (a) O K_1 and (b) UPS valence band spectra for $HfTiO_4$, or equivalently an Hf titante alloy with 1:1 composition of HfO_2 and TiO_2. The arrows in (a) and (b) indicate the smaller shifts in the π-bonded states at the top of the valence band and bottom of the conduction, as well as the larger shifts in the σ-bonded states at the bottom of the valence band and at higher energies in the conduction band.

B. La and Other RE Scandates

Qualitatively similar behavior are presented for stoichiometric La, Dy, and Gd scandates. Sc $L_{2,3}$, La $M_{2,3}$ and O K_1 spectra are presented in Fig. 13(a), (b), and (c), respectively, for $LaScO_3$ or equivalently $(La_2O_3)_1(Sc_2O_3)_1$ that has been annealed at 1000 °C in an inert ambient. The Sc $L_{2,3}$ spectrum in Fig. 13(a) displays a Jahn–Teller term-splitting similar to those of the Ti spectrum for Zr_2TiO_6 in Fig. 11(a), where the

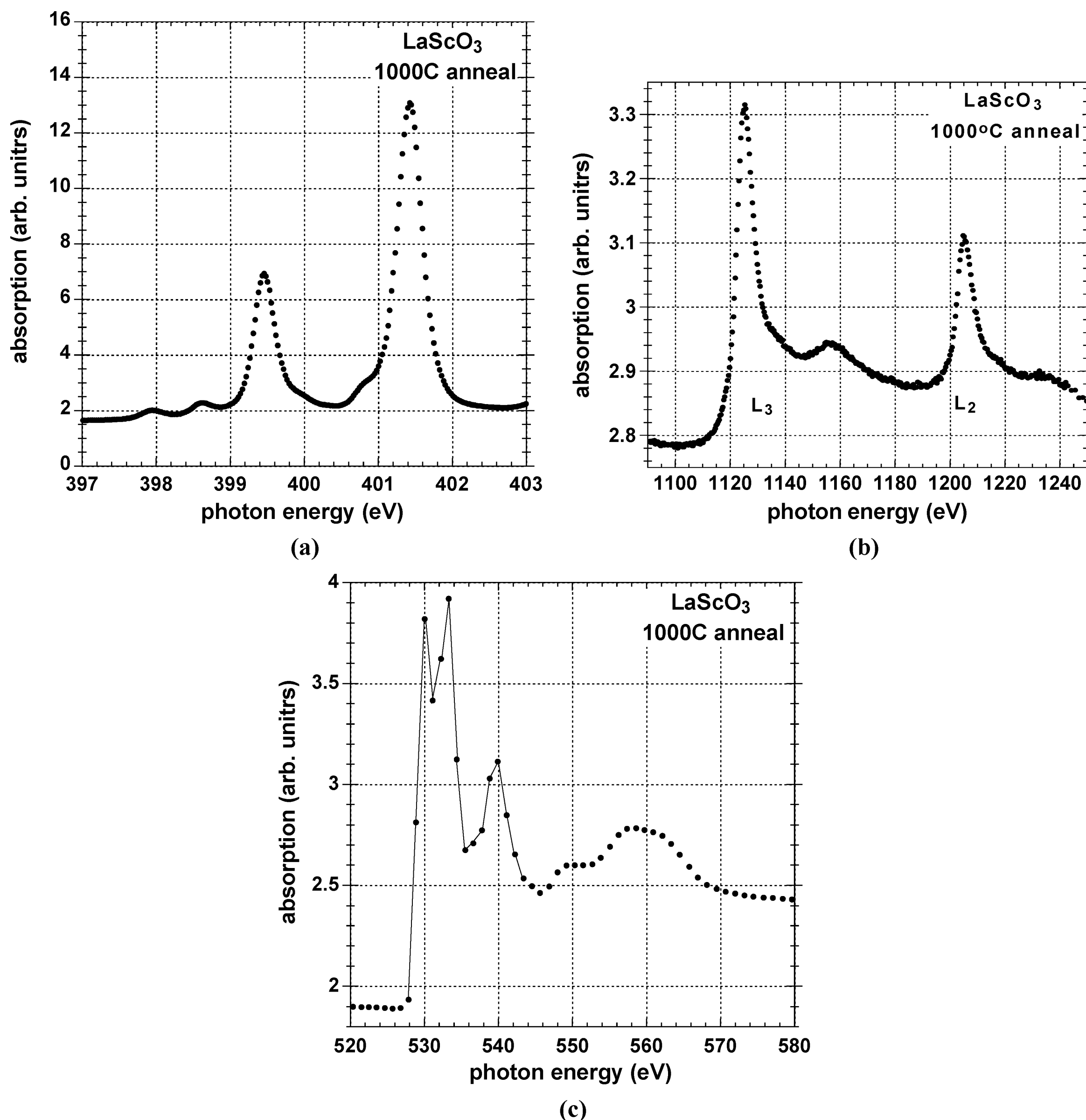

Fig. 13. Core level XAS spectra for nanocrystalline $LaScO_3$ or equivalently $(La_2O_3)_{0.5}(Sc_2O_3)_{0.5}$ that has been annealed at 1000 °C in an inert ambient: (a) Sc $L_{2,3}$ spectrum, (b) La $M_{2,3}$ spectrum, and (c) O K_1 spectrum.

term-splitting of the E_g feature is indicative of ionic bonding. The T_g term-splittings are 0.80 ±.05 eV, and are approximately the same as in TiO_2 and the Zr and Hf titanate alloys; however the *average* $T_{2g} - E_g$ or crystal field splitting is less, ∼2.7 eV as compared to 3.1 eV.

The La $M_{2,3}$ spectrum is displayed in Fig. 13(b). There is only one 5d feature in each of the spin-orbit split spectra. This is confirmed by taking a derivative spectrum, and also by comparison with the La $M_{2,3}$ spectrum in $LaAlO_3$, where each of the spin orbit spectra shows multiple La 5d states. The combination of spectroscopically resolved Jahn–Teller splittings in the Sc $L_{2,3}$ spectrum in Fig. 13(a) and the absence of Jahn–Teller splittings in the La $M_{2,3}$ spectrum in Fig. 13(b) is consistent with a nanocrystalline morphology based on the perovskite structure. In this structural model, there are x, y and z displacements of the Ti atom respect to its six O-neighbors, but the La atom remains in a symmetric environment with twelve nearest-neighbor O-atoms. The crystalline nature of this film has been verified by x-ray diffraction (XRD) [22].

The interpretation of the Sc $L_{2,3}$ and La $M_{2,3}$ spectra are consistent with the multiplicity of features in the O K_1 edge in Fig. 13(c). The spectra obtained to date are survey spectra at a lower spectral resolution than those obtained previously for crystalline $GdScO_3$ and $DyScO_3$ [9], and thin film $DyScO_3$ (not shown); however the O K_1 spectrum for the 1000 °C annealed film is consistent with the assignments made for Gd and Dy scandate O K_1 spectra in [2]. The feature at ∼538 to 540 eV in the $LaScO_3$ O K_1 spectrum is interpreted as the La 5d feature with a five-fold degeneracy similar to what has been found in the La $M_{2,3}$ spectrum. The lower energy features at ∼530 eV and 532 eV are corresponding to the two *strongest features* in the Sc $L_{2,3}$ spectrum at ∼399.4 and 401.4 eV. The splitting between these features in the Sc $L_{2,3}$ spectrum is $\sim 2.0 \pm 0.1$ eV, and approximately 2.2

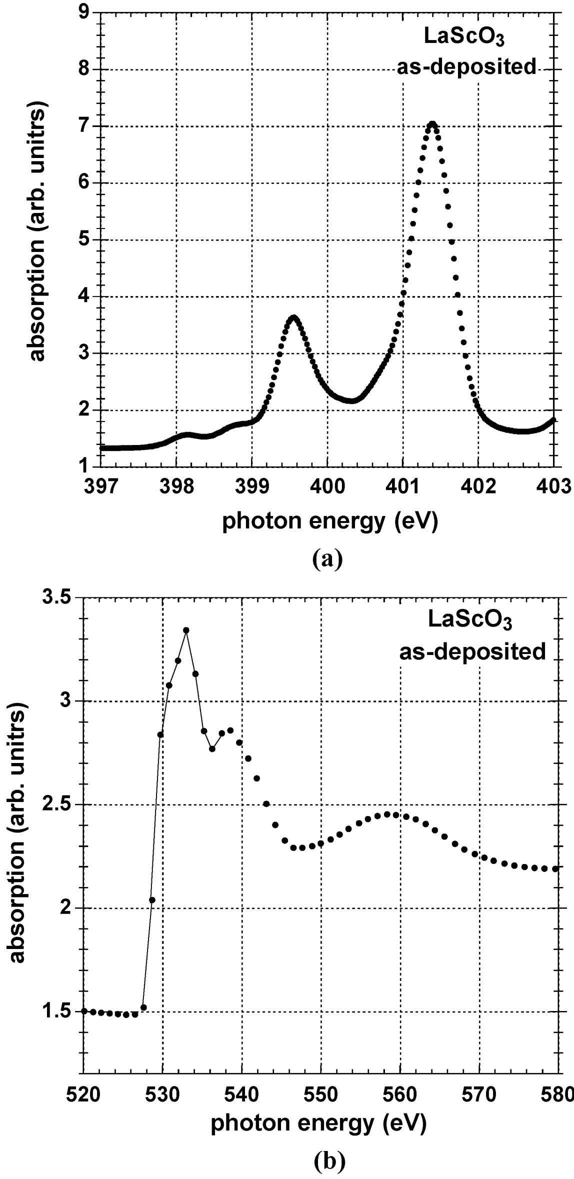

Fig. 14. Core level XAS spectra for as-deposited nanocrystalline $LaScO_3$: (a) Sc $L_{2,3}$ spectrum, and (b) O K_1 spectrum.

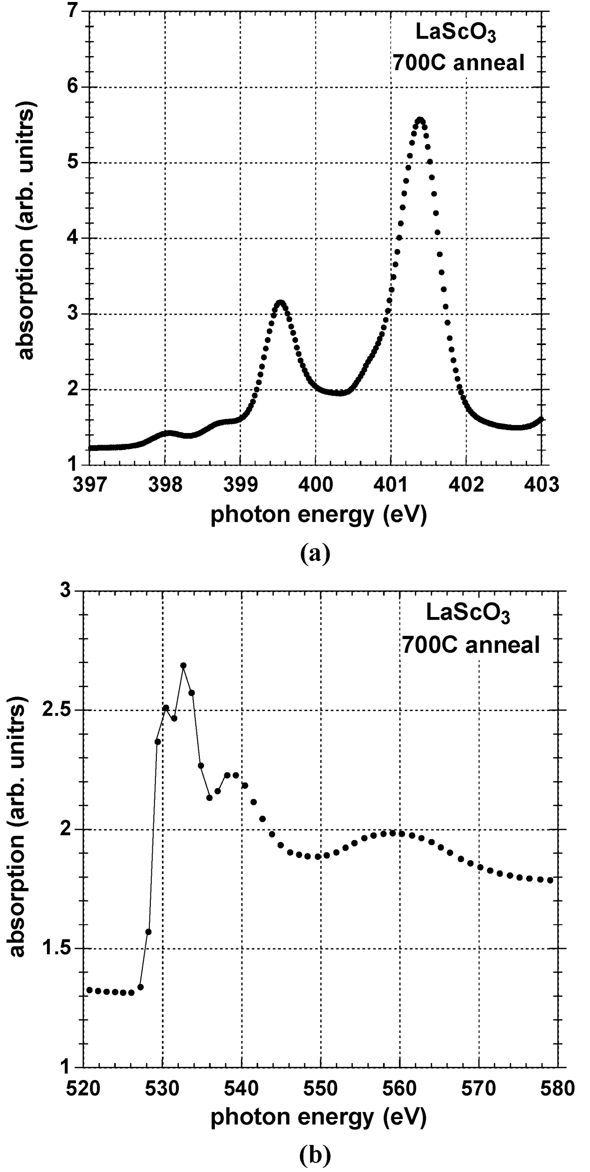

Fig. 15. Core level XAS spectra for nanocrystalline $LaScO_3$ that has been annealed at 700 °C in an inert ambient: (a) Sc $L_{2,3}$ spectrum, and (b) O K_1 spectrum.

± 0.25 eV in the O K_1 edge. This interpretation is consistent with the interpretation of the Zr titanate spectra discussed above; i.e., the TiO_2-like features in the O K_1 edge have a separation that is essentially the same as the separation between the two strongest features in the Ti $L_{2,3}$ spectrum.

Fig. 14(a) and (b) shows the Sc $L_{2,3}$ and the O K_1 edge spectra for as-deposited films, while Fig. 15(a) and (b) shows the same spectra for films annealed at 700 °C. The term-splittings in the Figs. 14(a) and 15(a), as well as the absence of term, or crystal field splitting the correspond as-deposited and 700 °C annealed La $M_{2,3}$ spectra (not shown) confirm the nanocrystalline nature of these films. XRD studies have detected crystallinity after an 850 °C anneal, but not in as-deposited or 700 °C annealed samples. This establishes that the XAS spectra are more sensitive to nanocrystallinity than XRD [22]; e.g., XRD can detect nanocrystallinity at a scale greater than 5 nm, but not at scale of less than 3 nm.

V. Discussion

A. Spin Orbit, Crystal Field, and Jahn–Teller Term Splittings

There are quantitative differences between: 1) spin-orbit splittings in core and valence d-states, and 2) d-state splittings that result from the electrostatic fields of near-nearest and more distant neighbors. Spin-orbit splittings dominate in core states, with the splitting increasing as the atomic number of the atom increases and the principal quantum number decreases. In contrast spin orbit splittings in valence p- and d-states are typically much less than 1 eV, and are lower by factors of at least two to crystal field spittings. Fig. 1 indicates a schematic representation of the crystal field and Jahn–Teller reductions in atomic d-state degeneracies that result from nearest neighbor bonding, and reductions/distortions in nearest-neighbor bonding and beyond that result from the static Jahn–Teller effect [2], [3], [15]. A cluster model to be published elsewhere, based on the Ph.D.

dissertation of one of the co-authors [11], has been proven useful in tracking some of the changes in d-state character in Fig. 6.

For example, when applied to ZrO_2, a cluster based on tetrahedral coordination give a smaller 4d crystal field splitting than a cubic eight-fold coordination cluster, ~1.9 eV as compared to 2.7 eV, scaling approximately as the square root of the number of nearest neighbor O atoms. Additionally, when applied to TiO_2, a cluster based on a distorted octahedral bonding arrangement that replicates the local atomic structure in rutile, removed the respective T_{2g} and E_g symmetries, and gave Jahn–Teller term splitting in good agreement with the Ti L_3 spectra of Figs. 3(a), 6, 10(a) and 11(a).

The cluster calculations do not consider spin orbit coupling, and since they gave very good agreement with experiment, this supports the argument that crystal field and Jahn–Teller term splittings dominate in valence band and conduction d-state energies in TM metal oxides, i.e., the crystal field and Jahn–Teller term splittings are greater than 0.7 eV in Ti and Sc 3d-states, Zr 4d and for Hf 5d states.

B. XAS Spectra of Elemental Oxides and Silicate Alloys

Differentiated O K_1 spectra for films of ZrO_2 and HfO_2 prepared by remote plasma assisted deposition and annealed at temperatures sufficient to drive out any water or carbon impurities indicate a multiplicity of d-state features. The respective multiplicities indicate that the E_g states are at the bottom of the conduction band, and therefore at the top of the valence band, and the T_{2g} states are higher in the conduction band, and deeper in the valence band [8]. The effective width of the valence band for ZrO_2 is approximately 6 eV for ZrO_2, and approximately the same for HfO_2 as well. The energy difference between the corresponding anti-bonding states in the respective O K_1 edges of ZrO_2 and HfO_2 are approximately the same and about 5 eV. The effective valence and conduction band widths are in excellent agreement with the calculations of [23].

The Jahn–Teller term-splittings in the ZrO_2 and HfO_2 O K_1 spectra are of the order of 1 eV, and these have not been detected in the Zr $M_{2,3}$ spectrum where two peaks are resolved, or in the Hf $N_{2,3}$ spectrum, where the crystal field splitting has not been resolved. A deconvolution of the ZrO_2 4d features in the Zr $M_{2,3}$ spectrum indicates a d-state splitting, $\Delta(d_1, d_2) = 2.2$ eV, and the full-width at half-maximum (FWHM) for each of these features is ~2.7 eV, which is well in excess of the spectral resolution of <0.3 eV of the measurement [6], [13]. Therefore the reason why term splittings are not observable in the Zr $M_{2,3}$ or Hf $N_{2,3}$ spectra is due to the short core life-time associated with the relatively high values of nuclear charge, 40 for Zr and 72 for Hf [12].

In marked contrast, the Jahn–Teller term splittings of for the Ti 3d states are not observable in the O K_1 spectrum, but are easily resolved in the Ti L_3 spectrum. The ability to observe multiple features in L_3 spectrum is a manifestation of a smaller value of $Z = 22$, whereas the inability to observe multiple features in the O K_1 may be correlated with the large difference in matrix elements for the Jahn–Teller term split T_{2g} states. It will demonstrated that these matrix element effects for the Jahn–Teller split T_{2g} states are also found in the absorption edge spectrum as probed by photoconductivity [16], or spectroscopic ellipsometry [24].

C. XAS Spectra of Complex Oxides

The XAS spectra of stoichiometric Zr and Hf titanates exhibit Jahn–Teller term splittings in the Ti $L_{2,3}$ spectra, but none are detected in the respective O K_1 spectra. This is consistent with what has been observed for TiO_2. In contrast La and other lanthanide RE scandates exhibit Jahn–Teller term splittings in the Sc $L_{2,3}$ and O K_1 edge spectra, but not in the La, Dy or Gd $M_{2,3}$ spectra. These results suggest an *empirical rule* for Jahn–Teller term splittings in complex oxides that contain only TM and/or RE oxides. The bonding distortions that are favored by the Jahn–Teller effect occur in the atomic species with the *lowest atomic d-state energy with respect to vacuum*. Based on a computation by Harrison [14], the respective d-state energies of Ti, Zr and Hf are −11.05 eV, −8.46 eV and −8.14 eV, while those for: 1) Sc are −9.35 eV, and 2) La, Gd and Dy, are approximately −6 to −6.6 eV.

In the case of the scandates, the distortion also occurs at the atomic site with the lowest O atom coordination, six-fold coordinated Sc, and not at the site with the higher O atom coordination, twelve-fold coordinated La, Gd or Dy. Similar considerations based on relative d-state energies also apply to *stoichiometric titanates* in the binary oxide systems: $ZrO_2 - TiO_2$ and $HfO_2 - TiO_2$; however, there have been fewer studies of these binary oxide phase diagrams to identify all of the possible titanate phases, and in addition to determine the coordinations of the Ti and Zr atoms. In this regard, Ti in combination with O-atoms is usually six-fold coordinated, but Zr and Hf display both six- and eight-fold coordination as for example in $PbZr(Hf)O_3$ and $Zr(Hf)O_2$, respectively [4].

D. Correlations Between XAS and Band Edge Spectra

The term splittings in the O K_1 spectra of HfO_2 and ZrO_2, and in the L_3 spectrum of TiO_2 have also been detected in the photoconductivity (PC) studies in [16], [26] and [27], and the vacuum ultra-violet spectroscopic ellipsomentry (VUV SE) studies of S. Zollner and co-workers [24], [25].

The majority of the spectral features attributed to *band tail states* in the PC and IPE spectra published in [16] and [26] are associated with band edge Jahn–Teller term split states discussed above. Fig. 16(a)–(d), are plots of the PC data for ZrO_2, HfO_2, TiO_2 and Al_2O_3 in Fig. 1 of [16], that emphasize the band tail region. The band tail region of the PC spectrum of Al_2O_3 is also included in Fig. 16(d) for comparison.

The PC spectra for ZrO_2 in Fig. 16(a) is for a thicker sample (~100 nm) than that of HfO_2 (~20 nm) and clearly reveals two photoconductivity edges, one at ~5.6 eV that defines the onset set of strong optical absorption that has been used to define the nominal bandgap of ZrO_2, and second, much weaker edge at about 5.0 eV that has not been assigned in any previous studies. This feature is also present in the VUV SE spectrum of ZrO_2, and a specific structural/bonding assignment will be made in the next section of this paper.

The data for HfO_2 in Fig. 16(b) also reveals two PC edges, one at ~5.9 eV that defines the onset of strong optical absorption that has been used to define the nominal bandgap of HfO_2,

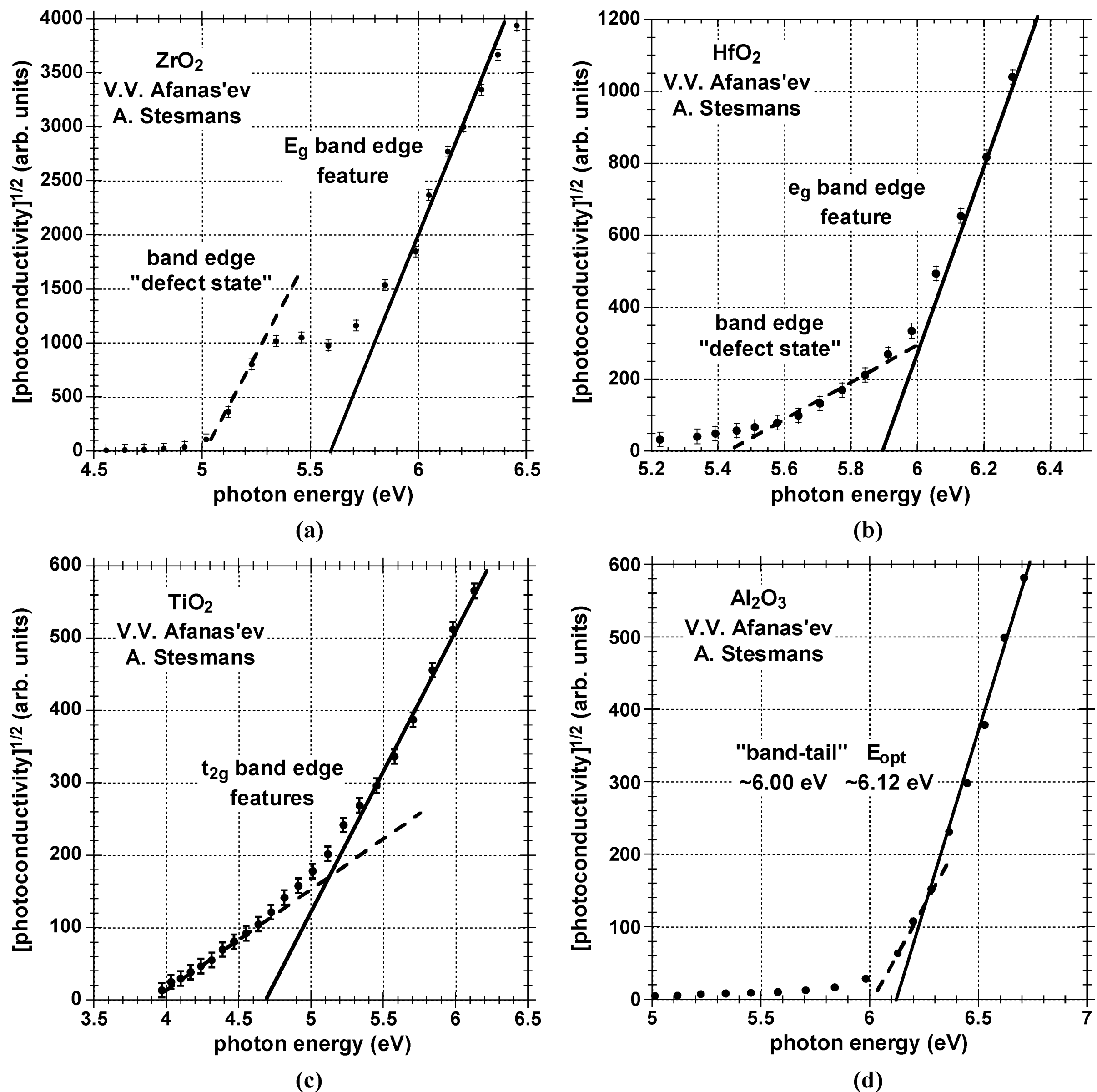

Fig. 16. Photoconductivity (PC) versus photon energy from [27] for (a) ZrO_2, (b) HfO_2, (c) TiO_2 and (d) Al_2O_3 plotted to emphasize the weaker features (dashed lines) below the strong features (solid line) that define the onset of strong PC and optical absorption.

and second, significantly weaker edge at about 5.4 eV that has not been assigned in any previous studies. Studies of the thickness dependence of the edge feature in ZrO_2 are consistent with assigning the respective features in ZrO_2 at ~5.0 eV and HfO_2 at ~5.45 eV to *the same microscopic "defect state."* It is important to distinguish between band edge tail states that are due to disorder, as in the case on noncrystalline Al_2O_3 in Fig. 16(d), and localized defect states as in ZrO_2 and HfO_2 in Fig. 16(a) and (b), respectively. The extent of the disorder induced band tailing in Al_2O_3 is ~0.15 eV, and the band edge defect states show a distinct edge behavior, particularly in the thicker ZrO_2 film. This is evident in Fig. 2 of [27], which shows the PC of ZrO_2 as a function of film thickness.

The data in Fig. 16(c) for TiO_2 indicate two edges, one at ~4.7 eV that marks the onset of strong optical absorption, and another at ~3.9 eV. The optical absorption at the band edge of 3.1 eV is too weak to show up in these PC studies on thin film samples [15]. The two edges in this PC spectrum for TiO_2 are assigned to intrinsic absorption states of TiO_2; this assignment is supported by the VUV SE studies of the next section.

Finally, the PC studies of complex RE scandates in [26] display strong band tailing at energies below those *generally assigned* to the fundamental band edge. This traditional assignment of a bandgap is incorrect, and does not take into account strong matrix element effects for the band edge states of the RE scandates. This behavior for the scandates parallels the behavior for TiO_2 and also has its origin in large differences matrix elements of Jahn–Teller term split states of octahedrally distorted bonding environments.

The PC spectrum of two representative scandate thin films, $LaScO_3$ and $DyScO_3$, are presented respectively in Fig. 17(a) and (b). Each of these films displays three quantitatively and qualitatively similar edge features at ~5.6 to 5.7 eV, 5.1 to 5.2 eV and ~4.5 eV. Comparisons between these features and the

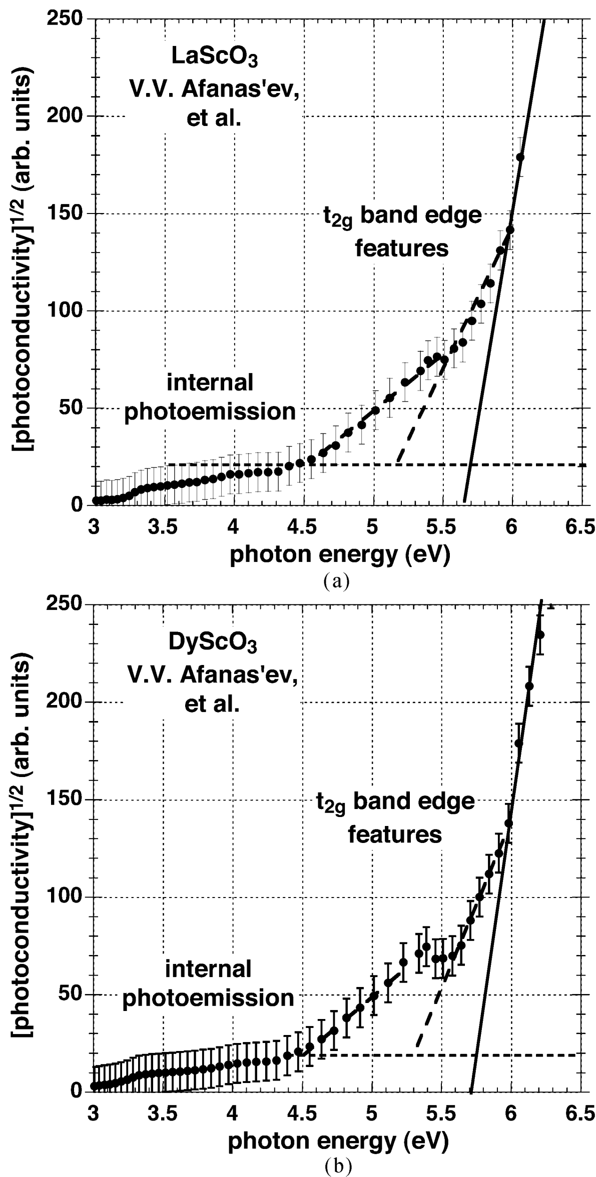

Fig. 17. Photoconductivity (PC) versus photon energy from [26] for (a) $LaScO_3$ and (b) $DyScO_3$ plotted to emphasize the weaker features (dashed lines) below the strong features (solid lines) that define the onset of strong PC and optical absorption.

term splittings of the Sc T_{2g} states that define the lowest conduction band edge indicate that they are intrinsic band edge states of the scandate complex oxides, and are transitions that originate in Sc π-bonding d-states in the valence band, and terminate in Sc π-anti-bonding d^*-states of the conduction band. As noted above these Sc d-states are coupled to O 2p states in the valence and O $2p^*$ states in the conduction band. In previously published papers, the strongest PC edge feature at ~5.6 to 5.7 eV was used to define the conduction band edge in RE scandates. This assignment is simply incorrect. In this regard it is significant to note that the onset of strong absorption in crystalline Sc_2O_3 occurs at about 6 eV, but there is an absorption tail that extends to about 4.6 eV [28]. Ref. [28] *incorrectly defines* the marked increase in absorption at ~6 eV as the Sc_2O_3 bandgap, ignoring the absorption tail that extends to about 4.6 eV, and failing to make comparisons with the well-understood absorption spectrum TiO_2 [15].

The results presented in [9] for $GdScO_3$ revealed an onset for strong absorption between 5.5 and 6 eV as well as weaker absorption with a threshold extending to ~4.5 eV. Therefore the results for the RE scandates and Sc_2O_3 support the interpretation presented above, that the d-state energies of same TM and RE atoms in elemental and complex oxides are at approximately the same relative energies with respect to vacuum, and that these energies correlate monotonically, and approximately linearly with the respective atomic d-state energies in the s^2 atomic configuration tabulated by Harrison [14].

Fig. 18(a)–(c) display respectively the absorption constants, α, for TiO_2, ZrO_2 and HfO_2 nanocrystalline thin films calculated from the real and imaginary parts of the complex dielectric constant, $\varepsilon_c = \varepsilon_1 + i\varepsilon_2$ [24], [25]. The values of ε_c were obtained from a fit to the optical constants obtained from spectroscopic ellipsometry data in the spectral range from approximately 1 eV to 9.5 eV. The peaks in ε_2 better define the energies of the d-state features than do the relative maxima in α, and these have been indicated in Fig. 18(a)–(c). The peaks in α are shifted in energy because they include a contribution from ε_1 as well as ε_2. Before commenting on the additional band edge feature in each of these spectra, it is important to note that there is excellent agreement between the relative energies of these features, and those obtained from either the Ti L_3 spectrum for TiO_2, and the O K_1 spectra for ZrO_2 and HfO_2. This is illustrated in Fig. 19 in a plot that summarizes the energies of the Jahn–Teller term split d-state spectral features in the ε_2 spectrum of TiO_2 as a function of the energies of the empty d-state features in the Ti L_3 spectrum. The slope of this plot is 1.1 establishing the correlation between the XAS results and the band edge absorption. A similar scaling holds for the d-state features in the ε_2 spectra of ZrO_2 and HfO_2, and the term splittings of the two E_g and first T_{2g} features in the respective O K_1 spectra.

The absorption spectra plots for ZrO_2 and HfO_2 in Fig. 18(b) and (c) respectively display an additional feature below the d-state features that have been correlated with XAS spectra and assigned to bulk nanocrystallite Jahn–Teller term split d-states. The additional feature is assumed to be an intrinsic defect state, i.e., one associated with the constituent atomic species of these elemental oxides. Based on the relatively high values of ε_2 and equivalently α, for this feature, the concentration of these defects may be as high as 10^{20} cm^{-3}. This assumption assumes an atomic absorption cross section/Zr atom of $\sim 10^{-15}$ to 10^{-16} cm^{-2}. This in turn corresponds to a bulk crystallite absorption coefficient between about 2×10^5 and 2×10^6 cm^{-1}.

This high concentration of defects is consistent with grain-boundary defect states that derive from Jahn–Teller term splittings larger than those in the bulk of the nanocrystallites. In this model, the additional term split states result an increased bonding distortion at the Zr14 atomic sites at the grain boundary; e.g., 4–5 of the O nearest neighbors, and the second shell of Zr second neighbors may reside in one crystallite, and the remainder of the O and Zr neighbors in a second crystallite. Preliminary calculations based on x, y and z directed distortions of Ti and Zr atoms from octahedral and cubic symmetry support this model. For the case Ti, changing the z axis Ti-O bond length difference with respect to the in-plane bonding from a symmetric to an asymmetric distortion increases the

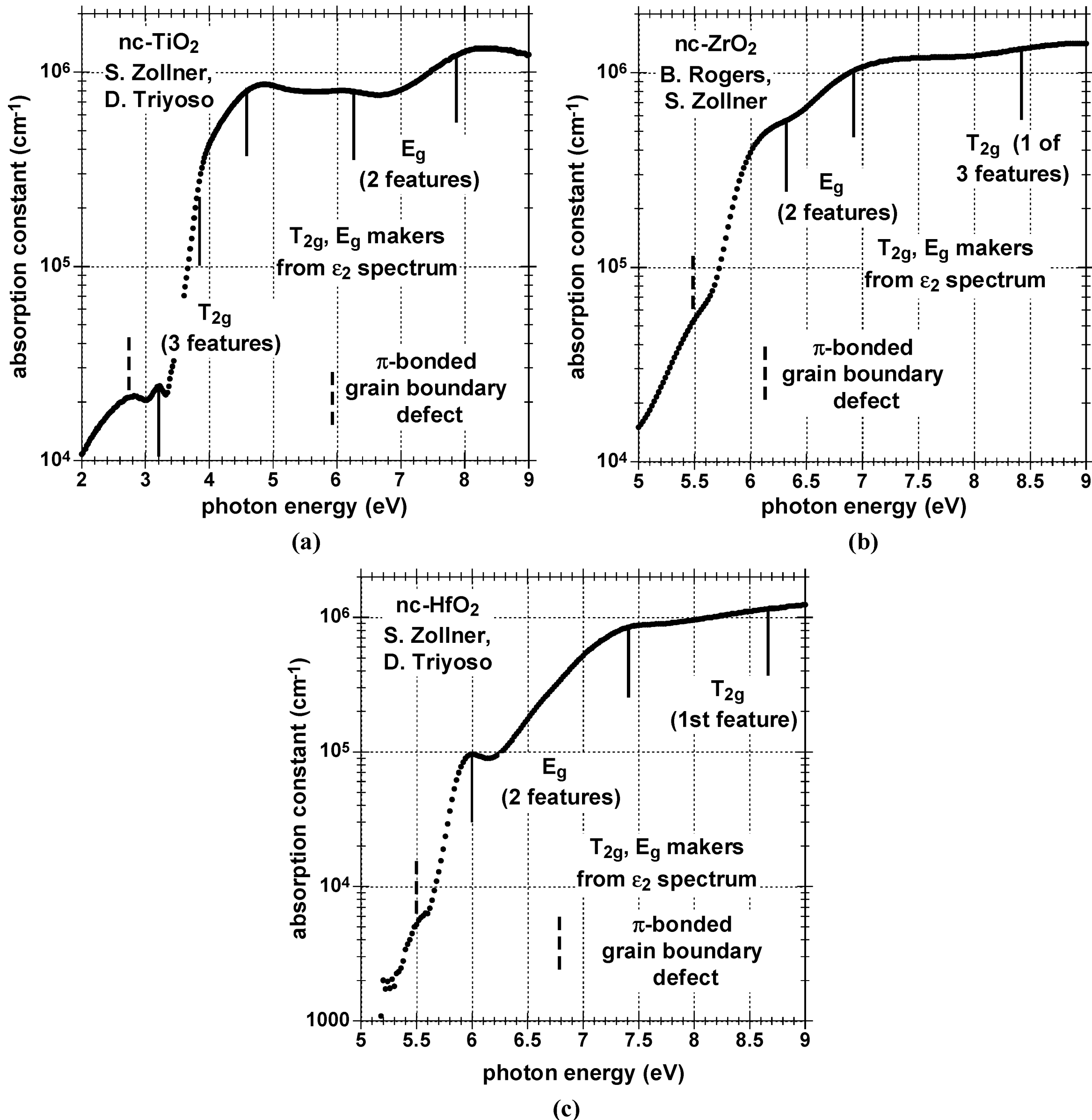

Fig. 18. Absorption constants, α, versus photon energy of nanocrystalline thin films (a) TiO_2, (b) ZrO_2 and (c) HfO_2 calculated from the real and imaginary parts of the complex dielectric constant, $\varepsilon_c = \varepsilon_1 + i\,\varepsilon_2$, as obtained from spectroscopic ellipsometry studies. The solid markers indicate the energies of features in the respective ε_2 spectra, and the dashed markers indicate the defect state associated with grain boundaries.

term splitting of the lowest π-bonded d-state. The inclusion of these grain boundary Jahn–Teller distortions has been included in the expanded crystal-field/Jahn–Teller term splitting diagram in Fig. 20.

This assignment is also consistent with PC data from [27], which are presented in Fig. 16(a) for ZrO_2 and (16b) for HfO_2. These plots use the data in [27], but with increased emphasis on the photoconductivity beyond the primary absorption edge. These onset of strong PC in each of these thin film materials occurs at the same photon energies, ~5.6 in ZrO_2 and 5.8 eV in HfO_2, as do the absorptions assigned to the lowest energy π-bonded E_g state at the respective band edges. The additional PC response at significantly reduced levels extends to lower photon energies, ~5.0 eV for ZrO_2 and ~5.4 eV for HfO_2. These PC features are at approximately the same photon energy as the band edge defect states in the respective absorption constant spectra. However, the magnitude of the PC reduced by a larger factor. This is consistent with a hopping transport through localized states rather than a band-transport in extended states.

There is a significantly larger difference in the optical absorption of the lowest π-bonded T_{2g} state in the absorption spectrum of TiO_2 than in those of ZrO_2 and HfO_2. This low value of absorption makes it difficult, if not impossible, to observe PC below about 4 eV in thin film TiO_2. This is indeed the case, and the PC edge in this material displays two thresholds, one at ~4.5 eV and the section at ~4 eV that are assigned, respectively to the 2nd and 3rd T_{2g} π-bonded states of the absorption edge as display in Fig. 18(c).

Complex RE scandates display similar band edge spectral features. Comparisons between the published absorption edge data for Sc_2O_3 [28], previously published studies of complex oxides, and the PC edge spectra of [26], display essentially the same behavior for the TM oxides. These similarities include the following: 1) the lowest lying conduction band states in Sc_2O_3

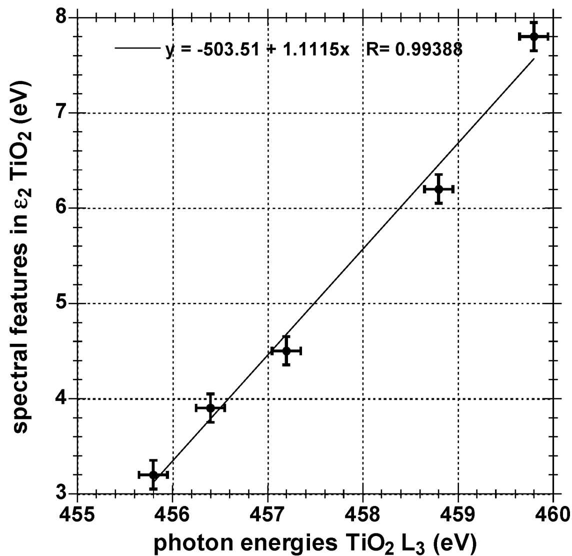

Fig. 19. Correlation between features of the L_3 edge and ε_2 for TiO_2.

from [28], and those revealed in XAS and PC spectra are approximately the same, with the effective band edge being determined by the lowest lying T_{2g} term split state of Sc at about 4.6 eV, and 2) the Sc T_{2g} state at $\sim$4.5–4.6 eV displays approximately the same relative reductions in optical and x-ray absorption strength as does the Ti T_{2g} state and TiO_2 band edge absorption at $\sim$3.1 eV [15].

PC spectra for representative RE scandates display essentially the same band edge, and band tail behavior as the TM oxides and this is illustrated in Fig. 17(a) for $LaScO_3$ and Fig. 17(b) for $DyScO_3$. The energies difference between the experimentally determined band edge states of $LaScO_3$ and TiO_2 is $\sim$ 1.6 ± 0.2 eV. This energy difference is approximately equal to the difference of $\sim$1.7 eV between their respective atomic state energies of -11.05 for Ti and -9.35 for Sc. The three PC thresholds at approximately 4.5 eV, 5.0 eV and 5.5 eV are assigned the Sc T_{2g} states at the band edge, and the PC below 4.5 eV is assigned to intrinsic defect states, some of which may be derived from Jahn–Teller term split states at internal grain boundaries.

Finally, similar Jahn–Teller term split features have been observed in $LaAlO_3$. Band edge features are due to Jahn–Teller effect associated with three fold degenerate Al 3p states, whereas in, there is a crystal field splitting the La 5d states as well. Consistent with a rhombohedral distortion in this perovskite the twelve-fold coordinated La atoms not longer reside in bonding site that complete spherical sysmmetry. This bonding is qualitatively different that the bonding of twelve fold coordinated Dy,Gd and La in the scandate perovskites that have an othrorhombic bonding distortion. This places the lowest bandgap of $LaAlO_3$ at $\sim$4.6 to 4.7 eV consistent with the absorption spectrum presented in [9] for a relatively thick single crystal sample.

VI. Summary: Alternative High-κ TM/RE Gate Dielectrics for CMOS Devices

There are several important insights made in this paper relative to the application of elemental and complex TM/RE oxides, and silicate and aluminate alloys in advanced Si devices. These new insights into band edge properties play a significant role in limiting the field of alternative dielectrics that can be integrated into bulk CMOS devices to extend the life-time of this approach to memory and logic integrated circuits and systems. Additionally, these limitations apply to use of these materials with semiconductor substrates other than Si as well, including trained Si-Ge, Ge and compound semiconductor.

A. Morphology of Deposited High-κ Gate Dielectrics

There has been much discussion about the character of deposited thin film dielectrics: are they amorphous, or nano- or polycrystalline? In a previous publication [29], one of the authors (GL) discussed a classification scheme based on bond-ionicity, and in the light of the spectroscopic studies reported in this review, it is important to review that approach, and indicate what has been learned in the years following the publication of that paper. The classification scheme was based on the well-established identification of three different bonding morphologies for glasses, and noncrsytalline solids in general: 1) continuous random networks, denoted here as CRNs; 2) disrupted or modified continuous random networks, denoted here as MCRNs; and 3) the random close packing of hard spheres, denoted here as RCPSs (random closed packed structures [30].

The prototypical CRN is noncrystalline SiO_2, in the vitreous or glassy form, and additionally as thermally grown or deposited thin films as well. The bonding is predominantly covalent, or equivalently less than 50% ionic as in SiO_2, where the Pauling bond ionicity, fi (or Ib) is 0.45 [29]. The bonding in these network structures follows the so-called 8-N rule [30], where N is the number of valence electrons. In SiO_2, $N = 4$ for Si and $N = 6$ for O, so that the Si atoms are four-fold coordinated in a tetrahedral bonding arrangement, and the O atoms are two-fold coordinated, bridging the Si atoms with a Si-O-Si bond angle of $\sim$148 degrees, and with a bond angle distribution of ± 10 degrees. The dihedral angles between tetrahedral groups are random, and this disorder, combined with the large Si-O-Si bond angle distribution provides the configurational entropy that is important in promoting glass formation and/or noncrystallinity in thermally grown or deposited thin films.

Other CRNs include SiO_2 solid solutions with boron oxide, B_2O_3 or phosphorous oxide, P_2O_5, silicon nitride, Si_3N_4, and silicon oxynitride alloys, which are solid solutions of SiO_2 and Si_3N_4. The solid solution CRNs are differentiated from the MCRNs because each of the individual alloy constituents, e.g., B_2O_3 or P_2O_5, form CRN structures as well. The highest values of κ attainable in low defect CRNs are approximately 5.5 and have been obtained in Si oxynitride alloys with approximately equal concentrations of SiO_2 and Si_3N_4 [31].

The prototypical MCRNs are silicates. These are also mixtures of oxides, but in this instance, the alloy constituents by themselves do not form CRN structures. Typical silicate alloys include mixtures of SiO_2 and 1) sodium oxide, Na_2O; 2) calcium oxide, CaO; 3) magnesium oxide, MgO; 4) PbO_2, lead dioxide; and 5) Al_2O_3, aluminum oxide to name just a few of the many silicates that have been studied.

Each of these oxides has a significantly higher bond ionicity that SiO_2, ranging from about 0.57 for Al_2O_3 to about 0.8 for

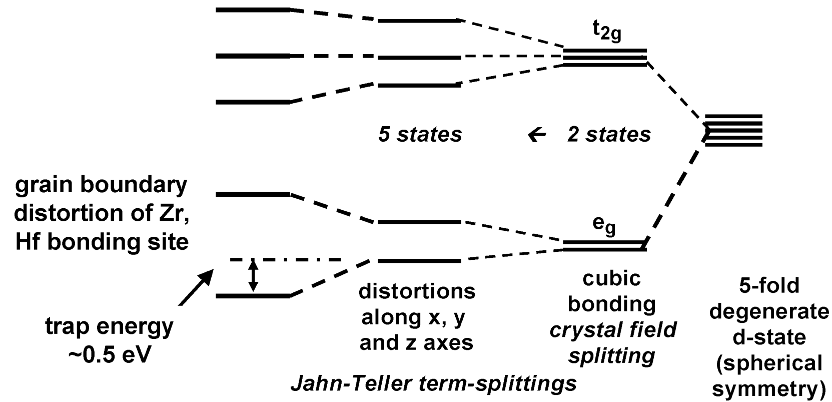

Fig. 20. Schematic representation of the Jahn–Teller distortions in TM elemental and complex oxides with eight-fold coordination, including the grain-boundary defect states.

Na_2O. The electro-positive atoms, Na, Ca, Mg, etc., are incorporated in ionic bonding arrangements in which their bonding coordinations are the same as they are in the ionic constituent oxides, e.g., six for Na and Ca. The bonding arrangements require the formation of electrostatic bonds that involve the nonbonding electrons on the bridging O atoms of the nondisrupted portion of the SiO_2 network, thereby increasing the average coordination of these atoms from two to three. These arrangements therefore disrupt the CRN through the formation of ionic bonding arrangements, and modify the network through the increase in the coordination of the network oxygen atoms as well.

In addition to the silicates listed above, silicates can also be formed by combining SiO_2 with TM oxides, such as ZrO_2, HfO_2, Y_2O_3 and La_2O_3, as well as trivalent rare earth atoms. Thin film TM and RE silicates have received attention as candidate materials for high-κ applications. They suffer from one significant draw back that is common to all silicate alloys; they chemically phase separate at elevated temperatures, e.g., about 900 °C, form two-phase mixtures of noncrystalline SiO_2, and nano- or microcrystallites of the more ionic oxide component [32].

There is also a body of experimental results that suggests that Al_2O_3 and Ta_2O_5 form noncrystalline thin film solids when deposited or grown from the vapor phase. However, these materials as well crystallize at relatively low temperatures, 800 to 900 °C [32]. The highest values of obtained in these MCRNs are generally in the range of 10, and in some instances up to about 15.

The third class of noncrystalline materials are RCPSs, which consist primary of metal alloys such as $Gd_{36}Fe_{64}$ and $Tb_{33}Fe_{67}$, and metal-metalloid alloys such as $Ni_{76}P_{24}$ and $Co_{78}P_{22}$ [30], [33]. These alloys have been prepared by rapid quenching of liquids, and by vacuum deposition of thin films. These alloys exhibit a unique feature in the radial distribution functions (RDFs) obtained from Fourier transform the x-ray scattering intensity (I(k)) as a function of wave vector, k. This is doublet in the second neighbor distance that corresponds to two different packings of hard spheres corresponding to: 1) in-line packing, in which two spheres of are each in direct contact with, and separated by a third sphere, and 2) a second packing arrangement in which the two spheres that separate a pair of spheres are in direct contact with each other and separate their two common neighbors. These two packing arrangements which can be permutted between the two components of a metallic alloy provide configuration entropy which contributes to glass formation.

The bond ionicity between the alloy components of these RCPSs is generally very small, less than 10% and does not mitigate the gains in the Gibbs free energy derived from the configuration entropy contributions.

One the other hand bond ionicities in excess of 65% for TM and RE oxides, and complex oxides make RCPSs energetically unfavorable because of Coulomb repulsions that completely mitigate the gains in configuration entropy form permutted packing arrangements such as those described above.

Therefore, as discussed above, when chemically pure, the morphology of TM and RE oxides, and TM and RE complex oxides will be crystalline. These materials are generally nanocrystalline as deposited, and crystallite sizes grow rapidly as annealing temperatures are increased above 700 °C. If the crystallites are less than about 3 nm in average in as-deposited, these cannot be detected by x-ray diffraction (XRD), and these films have termed “x-ray amorphous”. However, other techniques such as x-ray absorption, as discussed above, can detect nanocrystallinity through Jahn–Teller term splittings.

B. Band Gap and Conduction Band Offset Energy Scaling

Band gap scaling has been addressed above in the context of the seminal papers of John Robertson that combine model calculations with a limited amount of experimental data [2]. The experimental results presented in this paper reinforce the conclusions addressed above, and discussed in other publications [6]. The conclusion is that the bandgaps of high-κ TM/RE elemental oxides scale as the d-state energy of the respective TM/RE atoms. As noted in [6], this scaling may not apply to Y_2O_3 and La_2O_3 due to overlap with their respective 5s and 6s states. However, the limitation discussed above remains the same: the bandgaps and conduction band offset energies of the elemental high-κ dielectrics with highest static dielectric constants, Sc_2O_3, TiO_2, Ta_2O_5 and Nb_2O_5 have bandgaps and conduction band offset energies too small for use as alternative gate dielectrics in advanced Si devices.

Based on comparisons between the XAS spectra and/or optical bandgaps of TiO_2 and Hf and Zr titanate alloys, and Sc_2O_3

and RE scandate alloys, the Jahn–Teller term spittings, the optical bandgaps and therefore the conduction band offset energies for these nanocrystalline materials are essentially the same as those for TiO_2 and Sc_2O_3 respectively, and therefore are too small for applications as alternative gate dielectrics in advanced Si devices.

Based on these scaling considerations, this restricts the field of high-κ materials that have the potential for use as gate dielectrics in advanced Si devices to Zr, Hf, Y, La, and trivalent lanthanide rare earth oxides, and their respective silicate and aluminate alloys. However, two other issues must be addressed relative to these dielectrics: 1) the thermal stability of noncrystalline silicate and aluminate alloys, and 2) intrinsic defect states derived from grain boundaries in nanocrystalline thin films.

C. Thermal Stability of Silicate and Aluminate Alloys

The silicate and aluminate alloys of Zr and Hf are generally noncrystalline or amorphous as-deposited, but display chemical phase separation at temperatures of approximately 900 °C. These result in the formation of a nanocrystalline ZrO_2 or HfO_2. This has two consequences: 1) in alloys with less than 50 molecular percent ZrO_2 or HfO_2, the diphasic character of the phase separated thin film materials reduces the static dielectric constants, and 2) in alloy with more than 50 molecular percent ZrO_2 or HfO_2, it leads to crystallization with internal grain boundaries. In either the case these phase-separated films do not meet electrical performance metrics for advanced Si devices.

Crystallization has been impeded by the incorporation of nitrogen in these films, however, many problems remain that related to process integration issues. These are beyond the scope of this paper and will not be addressed.

D. Grain Boundary Defects and Electrical Performance

Bias dependent trapping and trap-assisted direct tunneling have been reported in states conduction band edge states near the conduction band edge in stacks gate dielectrics comprised of a Si substrate, a thin SiO_2 interfacial buffer layer, and a gate dielectric of HfO_2 [20], [21]. The trap assisted tunnelling (TAT) has been reported for low levels of bias, $\sim$1 eV above the flatband voltage, for both substrate and gate injection, while, the trapping or Frenkel Poole (FP) transport has been reported only for substrate injection. These results have correlated these bias dependent electrical properties with a high density of traps near the conduction band edge. Based on these studies, the energy of the trapping sites has been estimated at 0.5 to 0.8 eV below the band edge for extended state transport. This estimated energy is in excellent agreement with the band edge defect state found in PC and absorption spectra, and assigned in this paper to grain boundary, Jahn–Teller term split states.

Other studies of trapping in HfO_2 based dielectrics: 1) have found identified bias voltage level dependent effects in bias temperature instabilities (BTI) for substrate injection of electrons [34], that are also consistent with a high density of trapping states below the conduction band edge, and 2) have demonstrated that the traps at the conduction band edge of HfO_2, estimated to be at a depth of 0.3 to 0.5 eV, are pre-existing and not generated as a result of carrier injection [20], [21], [35]. The densities of these band edge traps have been demonstrated to be at least 10^{12} cm^2, and more likely in excess of 10^{13} cm^3, corresponding to volume densities of at least 10^{18} cm^{-2}, and probably as high as 3–5 $\times$ 10^{19} cm^{-3}. Based on the spectroscopic studies reported above, these trapping states are assigned to the states in HfO_2 associated the spectral feature below the lowest energy Eg conduction band state, i.e., the state that extends to about 0.5 eV below the conduction band edge. This defect has been assigned to a state resulting from a Jahn–Teller term split state that arises from a local bonding environment for Hf atoms at a grain boundary that is more distorted than at a Hf site in the bulk of a nanocrystallite. The density of these defects, as estimated from the optical absorption, and the PC is at least 10^{19} cm^{-2}, and in the same general range as determined from the transport studies.

Similar band edge states have been found in ZrO_2, and in the complex scandate dielectrics. Frenkel–Poole transport has been reported in ZrO_2 dielectric films, and in Ta_2O_5 as well [1], [20], [21]. The spectroscopic studies of this paper suggest that bias-direction (substrate or gate) dependent trapping and/or trap assisted tunneling be studied in alternative gate dielectrics, particularly those that are known to be nanocrystalline.

In this regard, band edge trapping has not been reported in as-deposited Zr of Hf silicate alloys when these films have not been subjected to annealing that results in chemical phase separation and crystallization. This includes nitrided Zr and Hf silicate alloys. Nitridation of HfO_2 provides improvements in carrier mobility, and these may be associated with preservation of a noncrystalline morphology which would eliminat grain-boundary defects that derive from increased Jahn–Teller bonding distortions.

E. Where Do We Go From Here?

There are other factors to address in the extension Si CMOS devices, as well as in devices based on other semiconductor substrates including Si-Ge, Ge and compound semiconductors. The results discussed above identify the importance of intrinsic defect states in nanocrystalline thin films and that can arise from Jahn–Teller term split states at the conduction band edge. There is an ongoing debate relative to the future of bulk CMOS, and a transition to semiconductor on insulator (SOI), and three-dimensional devices.

References

[1] M. Houssa, *High-k Gate Dielectrics*, M. Houssa, Ed. Bristol, U.K.: Inst. Physics, 2004, ch. 1.1.
[2] J. Robertson, *J. Vac. Sci. Technol.*, vol. B 18, p. 1785, 2000.
[3] F. A. Cotton and G. Wilkenson, *Advanced Inorganic Chemistry*, 3rd ed. New York: Interscience, 1972, ch. 20.
[4] H. Krebs, *Fundamentals of Inorganic Crystal Chemistry*. London, U.K.: McGraw-Hill, 1968, ch. 9 and 10.
[5] S. Okada and O. Matsuoka, *J. Phys. Chem.*, vol. 91, p. 4193, 1989.
[6] G. Lucovsky, J. G. Hong, C. C. Fulton, Y. Zou, R. J. Nemanich, and H. Ade, *J. Vac. Sci. Technol*, vol. B 22, p. 2132, 2004.
[7] G. B. Rayner Jr., D. Kang, Y. Zhang, and G. Lucovsky, *J. Vac. Sci. Technol.*, vol. B 20, p. 1748, 2002.
[8] C. C. Fulton, G. Lucovsky, and R. J. Nemanich, *Appl. Phys. Lett.*, vol. 84, p. 580, 2003.
[9] S. G. Lim *et al.*, *J Appl. Phys.*, vol. 91, pp. 4500–4505, 2002.
[10] L. F. Edge *et al.*, *Appl. Phys. Lett.*, vol. 86, p. 4629, 2004.
[11] Y. Zhang, Ph. D. Dissertation, Dept. Physics, North Carolina State Univ., Raleigh, 2005.

[12] E. U. Condon and G. H. Shortley, *The Theory of Atomic Spectra*. Cambridge, U.K.: Cambridge Univ. Press, 1957, ch. V.
[13] G. Lucovsky *et al.*, *J. Vac. Sci. Technol.*, vol. B 20, p. 1739, 2002.
[14] W. A. Harrision, *Elementary Electronic Structure*, Singapore: World Scientific, 1999.
[15] P. A. Cox, *Transition Metal Oxides*. Oxford, U.K.: Oxford Science, 1992.
[16] V. V. Afanas'ev and A. Stesmans, *High-κ Gate Dielectrics*, M. Houssa, Ed. Bristol, U.K.: Inst. Physics, 2004, ch. 3.3.
[17] International Technology Roadmap for Semiconductors (2001). [Online]. Available: http://public.itrs.net
[18] G. Lucovsky and J. C. Phillips, *J. Vac. Sci. Technol.*, vol. B 22, p. 2089, 2004.
[19] G. Lucovsky, J. P. Maria, and J. C. Phillips, *J. Vac. Sci. Technol.*, vol. B 22, p. 2097, 2004.
[20] J.-L. Autran, D. Munteanu, and M. Houssa, *High-κ Gate Dielectrics*, M. Houssa, Ed. Bristol, U.K.: Inst. Physics, 2004, ch. 1.4.
[21] X. Zu, M. Houssa, S. De Gendt, and M. Hyens, *Appl. Phys. Lett.*, vol. 80, p. 1975, 2001.
[22] L. F. Edge *et al.*, presented at the Physics and Chemistry of Semiconductor Interfaces Conf., Bozman, MT, Jan. 2005.
[23] P. W. Peacock and J. Robertson, *J. Appl. Phys.*, vol. 92, p. 4712, 2002.
[24] S. Zollner and D. Tyrioso, private communication.
[25] S. Zollner and B. R. Rogers, private communication.
[26] V. V. Afanas'ev *et al.*, *Appl. Phys. Lett.*, vol. 85, p. 5917, 2004.
[27] V. V. Afanas'ev and A. Stesmans, *Appl. Phys. Lett.*, vol. 80, p. 1957, 2002.
[28] H. H. Tippins, *J. Phys. Chem Solids*, vol. 27, p. 1069, 1966.
[29] G. Lucovsky, *J. Vac. Sci. Technol.*, vol. A 19, p. 1553, 2001.
[30] R. Zallen, *The Physics of Amorphous Solids*. New York: Wiley, 1983, ch. 1 and 2.
[31] G. Lucovsky, *IBM J. Res. Dev.*, vol. 43, p. 301, 1999.
[32] G. Lucovsky, G. B. Rayner, and R. S. Johnson, *Microelectron. Reliab.*, vol. 41, p. 937, 2001.
[33] C. S. Cargill III and S. Kirkpatrick, *Structure and Excitations in Amorphous Solids*, G. Lucovsky and F. L. Galeener, Eds. New York: American Inst. Physics, 1976, p. 339.
[34] J. Lee and K. Onishi, *High-κ Gate Dielectrics*, M. Houssa, Ed. Bristol, U.K.: Inst. Physics, 2004, ch. 5.3.
[35] G. Bersuker *et al.*, *Microelectron. Reliabil.*, vol. 44, p. 1509, 2004.

Photographs and biographies of the authors not available at the time of publication.